

*Research Articles: Neurobiology of Disease*

## **Trem2 deletion reduces late-stage amyloid plaque accumulation, elevates the A $\beta$ 42:A $\beta$ 40 ratio, and exacerbates axonal dystrophy and dendritic spine loss in the PS2APP Alzheimer's mouse model**

<https://doi.org/10.1523/JNEUROSCI.1871-19.2019>

**Cite as:** J. Neurosci 2020; 10.1523/JNEUROSCI.1871-19.2019

Received: 1 August 2019

Revised: 8 December 2019

Accepted: 23 December 2019

---

*This Early Release article has been peer-reviewed and accepted, but has not been through the composition and copyediting processes. The final version may differ slightly in style or formatting and will contain links to any extended data.*

**Alerts:** Sign up at [www.jneurosci.org/alerts](http://www.jneurosci.org/alerts) to receive customized email alerts when the fully formatted version of this article is published.

Copyright © 2020 Meilandt et al.

This is an open-access article distributed under the terms of the Creative Commons Attribution 4.0 International license, which permits unrestricted use, distribution and reproduction in any medium provided that the original work is properly attributed.

1 **Title:** *Trem2* deletion reduces late-stage amyloid plaque accumulation, elevates the  
2 A $\beta$ 42:A $\beta$ 40 ratio, and exacerbates axonal dystrophy and dendritic spine loss in the  
3 PS2APP Alzheimer's mouse model

4  
5 **Abbreviated Title:** Trem2 mitigates A $\beta$  neurotoxicity in PS2APP mice

6  
7 **Authors:** William J. Meilandt<sup>1\*</sup>, Hai Ngu<sup>2</sup>, Alvin Gogineni<sup>3</sup>, Guita Lalehzadeh<sup>1</sup>, Seung-  
8 Hye Lee<sup>1</sup>, Karpagam Srinivasan<sup>1</sup>, Jose Imperio<sup>1</sup>, Tiffany Wu<sup>1</sup>, Martin Weber<sup>1</sup>, Agatha J.  
9 Kruse<sup>3</sup>, Kimberly L. Stark<sup>1</sup>, Pamela Chan<sup>5</sup>, Mandy Kwong<sup>5</sup>, Zora Modrusan<sup>6</sup>, Brad A.  
10 Friedman<sup>4</sup>, Justin Elstrott<sup>3</sup>, Oded Foreman<sup>2</sup>, Amy Easton<sup>1</sup>, Morgan Sheng<sup>1</sup>, David V.  
11 Hansen<sup>1\*</sup>

12  
13 Departments of <sup>1</sup>Neuroscience, <sup>2</sup>Pathology, <sup>3</sup>Biomedical Imaging, <sup>4</sup>Bioinformatics,  
14 <sup>5</sup>Biochemical and Cellular Pharmacology, and <sup>6</sup>Molecular Biology, Genentech, Inc., 1  
15 DNA Way, South San Francisco, CA 94080 U.S.A.

16  
17 \* Correspondence: hansen.david@gene.com, meilandt.william@gene.com

18  
19 Number of pages: 43

20 Number of figures: 13 (9 Main, 5 Extended Data)

21 Number of tables: 1 (Extended Data Figure 2-1)

22 Number of words (Abstract): 192

23 Number of words (Introduction): 618

24 Number of words (Discussion): 909

25  
26 Conflict of interest statement: All authors are or were employees of Genentech, Inc.,  
27 with interests in developing novel therapeutics for neurodegenerative diseases at the  
28 time of performing work for this manuscript.

29  
30 Acknowledgments: We thank Melissa Gonzales Edick and Joanna Yung for imaging  
31 support; members of the Genentech animal care staff, FACS lab, and RNA sequencing  
32 lab for other research support; and Chris Bohlen for helpful critique of the manuscript.  
33 Karpagam Srinivasan's current affiliation is Alector, South San Francisco, CA 94080. AJ  
34 Kruse's current affiliation is Univ. Washington, Seattle, WA 98195. Morgan Sheng's  
35 current affiliation is the Broad Institute of MIT and Harvard, Cambridge, MA 02142.

36

37 **ABSTRACT**

38 *TREM2* is an Alzheimer's disease (AD) risk gene expressed in microglia. To study the  
39 role of *Trem2* in a mouse model of  $\beta$ -amyloidosis, we compared PS2APP transgenic  
40 mice versus PS2APP mice lacking *Trem2* (PS2APP;*Trem2*<sup>ko</sup>) at ages ranging from 4 to  
41 22 months. Microgliosis was impaired in PS2APP;*Trem2*<sup>ko</sup> mice, with *Trem2*-deficient  
42 microglia showing compromised expression of proliferation/Wnt-related genes and  
43 marked accumulation of ApoE. Plaque abundance was elevated in PS2APP;*Trem2*<sup>ko</sup>  
44 females at 6-7 months, but by 12 or 19-22 months of age it was notably diminished in  
45 female and male PS2APP;*Trem2*<sup>ko</sup> mice, respectively. Across all ages, plaque  
46 morphology was more diffuse in PS2APP;*Trem2*<sup>ko</sup> brains, and the A $\beta$ 42:A $\beta$ 40 ratio was  
47 elevated. The amount of soluble, fibrillar A $\beta$  oligomers also increased in  
48 PS2APP;*Trem2*<sup>ko</sup> hippocampi. Associated with these changes, axonal dystrophy was  
49 exacerbated from 6-7 months onward in PS2APP;*Trem2*<sup>ko</sup> mice, notwithstanding the  
50 reduced plaque load at later ages. PS2APP;*Trem2*<sup>ko</sup> mice also exhibited more dendritic  
51 spine loss around plaque and more neurofilament light chain in cerebrospinal fluid.  
52 Thus, aggravated neuritic dystrophy is a more consistent outcome of *Trem2* deficiency  
53 than amyloid plaque load, suggesting that the microglial packing of A $\beta$  into dense  
54 plaque is an important neuroprotective activity.

55

56 **Significance statement**

57 Genetic studies indicate that *TREM2* gene mutations confer increased Alzheimer's  
58 disease (AD) risk. We studied the effects of *Trem2* deletion in the PS2APP mouse AD  
59 model, in which overproduction of A $\beta$  peptide leads to amyloid plaque formation and  
60 associated neuritic dystrophy. Interestingly, neuritic dystrophies were intensified in the  
61 brains of *Trem2*-deficient mice, despite these mice displaying reduced plaque  
62 accumulation at later ages (12-22 months). Microglial clustering around plaques was  
63 impaired, plaques were more diffuse, and the A $\beta$ 42:A $\beta$ 40 ratio and amount of soluble,  
64 fibrillar A $\beta$  oligomers were elevated in *Trem2*-deficient brains. These results suggest  
65 that the *Trem2*-dependent compaction of A $\beta$  into dense plaques is a protective  
66 microglial activity, limiting the exposure of neurons to toxic A $\beta$  species.

67

68 **INTRODUCTION**

69

70 Since the discovery of *TREM2* (triggering receptor expressed on myeloid cells 2)  
71 variants as genetic risk factors for Alzheimer's disease (AD) (Guerreiro et al., 2013;  
72 Jonsson et al., 2013), *TREM2* biology has become a focal point in research efforts to  
73 better understand how the innate immune system impacts Alzheimer's and other  
74 neurodegenerative diseases (Jay et al., 2017b; Ulrich et al., 2017; Yeh et al., 2017).  
75 However, whether *Trem2* exerts protective or detrimental functions in mouse models of  
76 AD-related neuropathology has been rather unclear (Gratuze et al., 2018; Hansen et al.,  
77 2018; Ulland and Colonna, 2018).

78

79 In transgenic models of cerebral  $\beta$ -amyloidosis, plaque load has been reportedly  
80 increased, decreased, or unchanged in mice that lack *Trem2*, depending on the model,  
81 age, and brain region being analyzed (Jay et al., 2017a; Jay et al., 2015; Parhizkar et al.,  
82 2019; Wang et al., 2015; Wang et al., 2016; Yuan et al., 2016). *Trem2* deletion in  
83 amyloidosis models has also been reported to either increase or decrease  
84 phosphorylation of the endogenous tau protein (Jay et al., 2015; Wang et al., 2016).  
85 Similarly, studies in neurodegeneration models driven by transgenic expression of the  
86 human tau protein have suggested disparate roles of *Trem2*. In the hTau model  
87 (Andorfer et al., 2003), *Trem2* deletion increased the amounts of tau phosphorylation  
88 and aggregation detected (Bemiller et al., 2017). In contrast, in the PS19 model  
89 (Yoshiyama et al., 2007) *Trem2* deletion had a protective effect, preventing tau-driven  
90 synaptic loss and atrophy in the hippocampus and entorhinal cortex, respectively (Leyns  
91 et al., 2017).

92

93 Transcriptional profiling studies have defined a disease/damage-associated microglial  
94 (DAM) activation state that is commonly observed in the brains of neurodegeneration  
95 models (Deczkowska et al., 2018; Friedman et al., 2018). The acquisition of the DAM  
96 state is *Trem2*-dependent in mouse models of AD, amyotrophic lateral sclerosis, and  
97 demyelinating disease (Keren-Shaul et al., 2017; Krasemann et al., 2017; Poliani et al.,  
98 2015; Wang et al., 2015). Some have argued that this state of microglial activation or

99 alarm is fundamentally protective (Keren-Shaul et al., 2017), while others have argued  
100 that this state is damaging and that returning microglia to their normal “homeostatic”  
101 state would be beneficial (Krasemann et al., 2017). It is conceivable that microglial  
102 TREM2 activity may be either protective or detrimental, depending on the disease stage  
103 and types of pathology present.

104

105 To clarify the role of Trem2 in  $\beta$ -amyloid-driven AD models, we studied the effects of  
106 *Trem2* deletion on microglial activation, plaque accumulation, and neuronal pathology in  
107 the PS2APP model across a wide range of ages and in both sexes. PS2APP mice  
108 develop amyloid plaque and attendant gliosis pathologies that increase with age, with  
109 female mice accumulating the pathology more rapidly than males (Ozmen et al., 2009).  
110 Here we report that the effects of *Trem2* deficiency on plaque load varied with age and  
111 sex, but notably, plaque accumulation was reduced at older ages in both female and  
112 male Trem2 knockout (PS2APP;Trem2<sup>ko</sup>) mice compared to age-matched Trem2 wild  
113 type (PS2APP;Trem2<sup>wt</sup>) mice. We consistently observed that the A $\beta$ 42:A $\beta$ 40 ratio was  
114 elevated, plaque morphology was more diffuse, and neuritic dystrophy histopathology  
115 was more marked in PS2APP;Trem2<sup>ko</sup> mice, even at older ages when total plaque was  
116 reduced. Additional analyses of PS2APP;Trem2<sup>ko</sup> mice at the 12-month age revealed  
117 ApoE-laden microglia, increased levels of soluble fibrillar oligomeric A $\beta$ , and elevated  
118 neurofilament-L in the CSF. By RNAseq, we observed that proliferation-related  
119 transcripts in PS2APP;Trem2<sup>ko</sup> microglia were reduced, particularly those encoding  
120 certain components and regulators of Wnt-related signaling. Collectively, our data  
121 indicate that Trem2-dependent microglial proliferation and activation attenuate the toxic  
122 effects of A $\beta$  toward neurons—i.e., the DAM state is mainly protective—and that  
123 measurements of neuronal pathology are more informative than plaque load as  
124 readouts of microglial modulation in models of  $\beta$ -amyloidosis.

125

126

127 **MATERIALS AND METHODS**

128

129 *Animals.*

130 All animal care and handling procedures were reviewed and approved by the Genentech  
131 IACUC and were conducted in full compliance with regulatory statutes, IACUC policies and NIH  
132 guidelines. Animals were housed in SPF (specific pathogen-free) conditions with 12h light/12h  
133 dark/day and maintained on regular chow diets. The Trem2<sup>tm1(KOMP)Vlcg</sup> null allele (C57BL/6N  
134 background) was crossed into the PS2APP model (C57BL/6J background). To generate  
135 experimental cohorts, all breeding mice were homozygous carriers of the PS2APP transgene  
136 and heterozygous carriers of the Trem2-null allele to allow maximal use of littermates between  
137 Trem2 wild type (Trem2<sup>wt</sup>) and Trem2 knockout (Trem2<sup>ko</sup>) PS2APP groups. We designed our  
138 study to analyze female cohorts at early (4 months), intermediate (6-7 months), and late (12  
139 months) stages of pathology. We also analyzed males at the age of 6-7 months—a common  
140 age for us to examine PS2APP histopathology—to check whether any observed effects of  
141 Trem2 deletion were sex-specific. The 4-month and 6-7 month cohorts were processed  
142 together; the 12 month and 19-22 month cohorts were separate batches. When we observed  
143 less plaque in 12mo PS2APP;Trem2<sup>ko</sup> females, we decided to also analyze their still aging male  
144 counterparts to learn whether that effect was reproducible. (By that time, the numbers of aged  
145 males were somewhat depleted so we included available Trem2<sup>het</sup> mice to round out the  
146 analysis.) For dendritic spine analysis, animals also carrying the Thy1:GFP-M transgene  
147 (Jackson stock 007788) were used.

148

149 *Flow cytometry and fluorescence activated cell sorting (FACS).*

150 Animals were anesthetized with ketamine/xylazine and transcardially perfused with 30  
151 ml of ice-cold PBS prior to dissection of cortex + hippocampus. Care was taken to remove the  
152 choroid plexus and as much of the meninges as possible prior to dissociation and sorting.  
153 Tissues were dissociated and cell suspensions prepared as described previously (Srinivasan et  
154 al., 2016). All steps were carried out on ice or at 4°C to prevent artifactual microglial activation.

155 For quantifying CD45 immunoreactivity and collecting brain-resident myeloid cells by  
156 FACS, cell suspensions from seven PS2APP;Trem2<sup>wt</sup> (5 females, 2 males) and seven  
157 PS2APP;Trem2<sup>ko</sup> (6 females, 1 male) mice at 14-15 months of age were stained with the  
158 following antibodies in Hibernate-A medium for 20 minutes at 4°C on a rotator: APC-conjugated  
159 anti-CD11b (BD Biosciences 561690, 1:200), PE/Cy7-conjugated anti-CD45 (BD Biosciences  
160 552848, 1:500), FITC-conjugated anti-Ly6g (Tonbo Biosciences 35-5931, 1:200), and PE-  
161 conjugated anti-Ccr2 (R&D Systems FAB5538P, 1:200). Samples were briefly washed and  
162 stained with DAPI prior to FACS sorting. Myeloid cells were selected by gating live (DAPI-  
163 negative) cells for CD11b and CD45 immunoreactivity. To avoid the presence of peripheral  
164 myeloid cells in the flow analysis and FACS collections, Ccr2<sup>+</sup> cells (peripheral  
165 monocytes/macrophages) and Ly6g<sup>+</sup> cells (neutrophils) were excluded. The total population of  
166 brain-resident myeloid cells (defined as CD11b<sup>+</sup>CD45<sup>+</sup>Ccr2<sup>-</sup>Ly6g<sup>-</sup>), consisting almost entirely of  
167 microglia but including CD45<sup>high</sup> perivascular macrophages (~2% of total), from each sample  
168 was collected in Hibernate-A. Collected cells were pelleted at 5,000 rcf for 8 minutes, and RNA  
169 was extracted from cell pellets using Qiagen RNeasy Micro kits. To measure CD45

170 immunoreactivity of brain myeloid populations during FACS, CD45<sup>low</sup> and CD45<sup>high</sup> gates were  
171 defined using a non-transgenic animal as a control to identify microglia in their normal state  
172 (CD45<sup>low</sup>). The same gates were transposed onto cells from PS2APP animals sorted on the  
173 same day in the same machine to ensure accuracy and consistency in determining percentages  
174 of CD45<sup>low</sup> and CD45<sup>high</sup> populations. Generally, animal pairs including one PS2APP;Trem2<sup>wt</sup>  
175 and one PS2APP;Trem2<sup>ko</sup> animal were processed together from perfusion through sorting. Data  
176 for non-transgenic animals in Fig. 1F includes the non-transgenic animals used to define the  
177 CD45 gates used during PS2APP cell sorting, as well as additional age-matched control  
178 animals from another cohort processed at another time (due to animal availability constraints).

179 For measuring microglial cells with  $\beta$ -amyloid content, animals at ~12 months (n=3  
180 PS2APP;Trem2<sup>wt</sup> and 2 PS2APP;Trem2<sup>ko</sup>) were intraperitoneally injected with methoxy-X04 (10  
181 mg/kg) 24 hours before tissue collection. Animals were processed as described above and  
182 dissociated cells were stained for CD11b. Cells were also incubated with Calcein-AM  
183 (eBioscience 65-0853-39, 1:1000) just prior to flow cytometry to label live cells using the 488 nm  
184 excitation channel. Live CD11b<sup>+</sup> cells were gated as X04<sup>+</sup> or X04<sup>-</sup> using the DAPI excitation  
185 channel to determine the percentage of microglia with ingested amyloid content. Transgenic  
186 animals injected with PBS were also used as negative controls (data not shown).

187

188 *RNA sequencing, differential expression and gene set analysis.*

189 RNA samples from sorted brain myeloid cells of seven PS2APP;Trem2<sup>wt</sup> (5 females, 2  
190 males) and six PS2APP;Trem2<sup>ko</sup> (5 females, 1 male) mice (14-15 months old) were selected for  
191 sequencing. The concentration of RNA samples was determined using DS-11  
192 spectrophotometer (DeNovix) and the integrity of RNA was determined by 2100 Bioanalyzer  
193 (Agilent Technologies). Approximately 1-5 ng of total RNA was used as an input material for the  
194 library generation using SMART-seq v4 Ultra Low Input RNA kit (Clontech). Size of the libraries  
195 was confirmed using 4200 TapeStation and High Sensitivity D1K screen tape (Agilent  
196 Technologies) and their concentration was determined by qPCR-based method using KAPA  
197 Library Quantification Kit. The libraries were multiplexed and then sequenced on HiSeq4000  
198 (Illumina) to generate 30M of single-end 50 bp reads. Sorted cell RNA-Seq data were analyzed  
199 as described (Srinivasan et al., 2016). Briefly, Illumina adapters, low-quality sequences, and  
200 rRNA reads were first discarded. Remaining reads were aligned to the GRCm38 genome with  
201 GSNAP aligner (Wu et al., 2016) and reads overlapping each gene were quantified.  
202 Normalization was based on the nRPKM method, which is proportional to size factor  
203 normalization of DESeq (Love et al., 2014). Differential expression was performed using  
204 voom+limma (Law et al., 2014). Raw RNA-Seq data have been deposited to NCBI GEO under  
205 accession number GSE140744.

206 Heat maps in Fig. 2A and Fig. 2-3 were generated using gene sets of interest to  
207 compare transcriptional responses in multiple datasets. Z-scores were calculated as follows.  
208 First, log<sub>2</sub>-scale expression matrices were calculated as  $\max(\log_2(\text{nRPKM}), -4)$ . Then, each  
209 gene was centered and scaled to give Z scores: for a given gene/sample combination, the Z  
210 score represents distance of nRPKM value in standard deviations from the mean log<sub>2</sub>-scale  
211 expression value for that gene across all samples within a dataset. Rows (genes) were

212 organized hierarchically using the Euclidean distance function. Columns (sorted microglia  
213 samples) were organized by project and genotype.

214 Gene ontology (GO) query was submitted on the PANTHER Classification System  
215 version 14.1 (Mi et al., 2019) at the website (<http://pantherdb.org/>) using the following inputs:  
216 Gene list = genes differentially expressed between Trem2<sup>ko</sup> and Trem2<sup>wt</sup> PS2APP microglia  
217 (fold change  $\geq 2$ , adj. p value  $\leq 0.05$ ); Organism = *Mus musculus*; Analysis = statistical  
218 overrepresentation test; Annotation set = GO biological process complete; Reference list = *Mus*  
219 *musculus* whole genome genes; Test type = Fisher's exact; Correction = Calculate false  
220 discovery rate.

221 For gene set enrichment analyses in Fig. 2D and Fig. 2-2, each sample was assigned a  
222 gene set score using  $\log_2(\text{nRPKM})$  values for each gene in the set. A sample's gene set score  
223 reflected the average difference, for all genes in the set, between that sample's measured  
224  $\log_2(\text{nRPKM})$  value for a given gene and the average  $\log_2(\text{nRPKM})$  value for the same gene  
225 across all samples. In cases when one or more samples had no transcripts detected for a given  
226 gene, an imputed  $\log_2(\text{nRPKM})$  value was assigned equal to one  $\log_2$  step below the lowest  
227  $\log_2(\text{nRPKM})$  value detected for that gene in that sample set. We compared gene set scores  
228 between genotype groups using two-tailed *t* tests assuming unequal variance between groups.  
229

#### 230 *Sectioning, histological and immunological staining.*

231 Single-sex cohorts of animals used for histological and biochemical analyses included 4-  
232 month (4mo) females (n=11 non-transgenic Trem2<sup>wt</sup>, 14 non-transgenic Trem2<sup>ko</sup>, 10  
233 PS2APP;Trem2<sup>wt</sup>, and 12 PS2APP;Trem2<sup>ko</sup>), 6-7mo females (n=11 PS2APP;Trem2<sup>wt</sup> and 13  
234 PS2APP;Trem2<sup>ko</sup>), 6-7mo males (n=16 PS2APP;Trem2<sup>wt</sup> and 14 PS2APP;Trem2<sup>ko</sup>), 12mo  
235 females (n=15 PS2APP;Trem2<sup>wt</sup> and 15 PS2APP;Trem2<sup>ko</sup>), and 19-22mo males (n=12  
236 PS2APP;Trem2<sup>wt</sup>, 8 PS2APP;Trem2<sup>het</sup>, and 7 PS2APP;Trem2<sup>ko</sup>). Animals were deeply  
237 anesthetized with 2.5% tribromoethanol (0.5 ml/25 g body weight) and transcardially perfused  
238 with PBS. One brain hemisphere was drop-fixed in 4% PFA for two days at 4°C with agitation  
239 and then transferred to PBS for histopathological analyses. The other hemisphere was  
240 subdivided into cortical and hippocampal tissues that were frozen and stored at -80°C for  
241 biochemical assays. Immersion-fixed hemi-brains were cryoprotected, embedded up to 40 per  
242 block in a solid matrix, and coronally sectioned at 35  $\mu\text{m}$  (MultiBrain processing by  
243 NeuroScience Associates) as previously described (Kallop et al., 2014; Wang et al., 2011).  
244 Sheets of sections were stored in cryoprotectant (30% glycerol, 30% ethylene glycol in PBS) at  
245 -20°C until use.

246 Immunohistochemical (IHC) stains for Iba1, CD68, and Gfap were performed at  
247 NeuroScience Associates as described previously (Wang et al., 2011), and CD68-stained  
248 sections were counterstained with Nissl (0.05% thionine/0.08 M acetate buffer, pH 4.5). Silver  
249 stains for amyloid plaque (Campbell-Switzer stain (Switzer et al., 1993)) and neuronal  
250 damage/degeneration (Amino Cupric Silver (AminoCuAg) or "Disintegrative Degeneration" stain  
251 (de Olmos et al., 1994)) were also performed at NeuroScience Associates. The bases for these  
252 silver stains are reviewed in (Switzer, 2000) and described on the NeuroScience Associates  
253 website (<https://www.neuroscienceassociates.com/technologies/staining/>). IHC and silver stains

254 spanned a broad rostral-caudal range including eight to eleven sections per animal. Stained  
255 slides were returned to Genentech for imaging and quantitation, and unused sections were also  
256 returned to Genentech for cryoprotected storage until used for additional stains.

257 For X-34 stains, sheets were mounted onto slides and completely dried. Slides were  
258 incubated with 10  $\mu$ M X-34 in PBS containing 40% ethanol and 0.02 N NaOH for 10 min,  
259 followed by 3 quick washes in PBS, differentiation in 80% ethanol for 1 min, and additional 3  
260 quick PBS washes. After applying ProLong Diamond Antifade Mountant (ThermoFisher  
261 P36961), slides were covered with no.1 coverslips. Two sections per animal were stained, with  
262 all cohorts stained and analyzed simultaneously.

263 For co-staining of plaque, microglia, and ApoE or dystrophic axons, sheets  
264 encompassing 2-3 sections per animal containing regions of the rostral and caudal  
265 hippocampus were washed in PBS and then PBS plus Triton X-100 (PBST, 0.1%) and then  
266 blocked in PBST (0.3%) with 5% bovine serum albumin (BSA) and 5% normal donkey serum,  
267 then incubated overnight with primary antibodies diluted in PBST (0.3%) plus 1% BSA at 4°C.  
268 Microglia were labeled with rabbit anti-Iba1 (Wako 019-19741, 1:000) or goat anti-Iba1 (Abcam  
269 ab5076, 1:1000), ApoE with a rabbit monoclonal antibody (Abcam ab183597, 1:4000), and  
270 dystrophic neurites with rat anti-Lamp1 (Abcam ab25245, 1:2000). Primary antibody incubation  
271 was followed by three 10-minute washes in PBST, followed by incubation with secondary  
272 antibodies for 2 hours at room temperature. Donkey anti-rabbit IgG-Alexa555, anti-rat IgG-  
273 Alexa647, and anti-goat IgG-Alexa647 (Thermo Fisher, 1:500) were used as secondary  
274 detection reagents. Following the stain, tissue sheets went through three 10-minute washes in  
275 PBST (0.1%) and three quick washes in PBS. Sheets were mounted onto slides with 0.1%  
276 gelatin in PBS and allowed to dry and adhere to the slide at room temperature. To label plaque,  
277 slides were then incubated with 10  $\mu$ M methoxy-X04 in 40% ethanol in PBS for 10 min, washed  
278 briefly in PBS, differentiated in 0.2% NaOH in 80% ethanol for 2 min, washed and then allowed  
279 to dry. Slides were coverslipped with added ProLong™ Gold Antifade Mountant (Thermo Fisher  
280 P36961). All cohorts were stained and analyzed simultaneously.

281

282 *Imaging and quantitation of stained sections.*

283 Brain tissue samples processed by NeuroScience Associates were imaged on the Leica  
284 SCN400 whole slide scanning system (Leica Microsystems, Buffalo Grove, IL) at 200x  
285 magnification. Matlab (Mathworks, Natick, MA) running on a high performance computing  
286 cluster was used for all whole slide image analysis performed in a blinded manner.  
287 Quantification of CD68 or Iba1 staining and enlarged dark cluster areas was performed using  
288 morphometric-based methods as previously described (Kallop et al., 2014; Le Pichon et al.,  
289 2013). The large dark “cluster” of CD68 or Iba1<sup>+</sup> cells coincided with the presence of amyloid  
290 plaques. Analysis of Amino Cupric staining was performed using color thresholds and  
291 morphological operations. Plaque area was analyzed from slides stained using the Campbell-  
292 Switzer method with plaques appearing with a black or amber hue. Multiple color classifiers  
293 spanning narrow ranges in RGB and HSV space were created for positive and negative features.  
294 Plaques were segmented using these classifiers and applying adaptive thresholding, Euclidean  
295 distance transform, morphological operations, and reconstruction. The percentage plaque load,

296 Amino Cupric, Iba1, CD68, or Gfap positivity for the entire section was calculated by normalizing  
297 the positive pixel area to tissue section area and averaged from eight to eleven sections/animal.  
298 All images, segmentation overlays, and data were reviewed by a pathologist.

299 Image acquisition of immunofluorescent slides costained for plaque, microglia, and  
300 either ApoE or dystrophic neurites was performed at 200x magnification using the Nanozoomer  
301 S60 or XR (Hamamatsu Corp, San Jose, CA) digital whole slide scanner. Ideal exposure for  
302 each channel was determined based on samples with the brightest intensity and set for the  
303 whole set of slides to run as a batch. Total tissue area was detected by thresholding on the Iba1  
304 signal and merging and processing of the binary masks by morphological operations. Methoxy-  
305 X04, Lamp1, ApoE and Iba1 staining was analyzed using a top-hat filter and local threshold  
306 followed by morphological opening and closing. For Lamp1 and methoxy-X04 staining, shape  
307 factor, roundness and solidity features were used to eliminate elongated objects. In addition, a  
308 minimum size of  $34 \mu\text{m}^2$  was applied to exclude small areas of staining. The detected plaques  
309 were used as markers in a marker-controlled watershed segmentation to create watershed lines  
310 of separation. The plaque mask was then dilated by  $17 \mu\text{m}$  but constrained to be within  
311 watershed lines to prevent merging of plaques in close proximity during dilation. Total Lamp1-  
312 positive staining was normalized to the whole tissue area. Plaque-associated Lamp1 and Iba1  
313 staining was constrained to be within the mask of dilated area around plaque and was  
314 normalized to the same area. Plaque-associated ApoE staining was constrained to be within the  
315 mask of plaque + dilated area and normalized to plaque area. Data was averaged from 2-3  
316 sections per animal.

317 For X-34 stains, images were collected with a confocal laser scanning microscope  
318 LSM780 (Carl Zeiss, Inc.) using Zen 2.3 SP1 software (Carl Zeiss, Inc.). 11 z-stack images at 1  
319  $\mu\text{m}$  intervals were collected with Plan-Apochromat 20X/0.8 M27 and maximum intensity  
320 projection images were created using Zen software. Images were collected and processed blind  
321 to genotypes. Image analysis was performed using Matlab in a blinded fashion on the maximum  
322 intensity projection of the confocal z-stack. Control images that did not have X-34 positive  
323 staining were used to determine an initial threshold to exclude background. A threshold that is  
324 greater than 99.99% of all pixel intensities in the control images was applied to all images to  
325 determine an initial segmentation mask. The binary masks were then smoothed out using  
326 morphological opening and closing. A minimum size of  $9 \mu\text{m}^2$  was applied to exclude small  
327 areas of staining. A threshold corresponding to the 80<sup>th</sup> and 50<sup>th</sup> intensity percentile for the  
328 pixels within the segmentation mask of all positive images was applied to analyze compact and  
329 diffuse area, respectively. Post-threshold morphological operations and size exclusion was  
330 performed as described above. The plaque diffuseness index was calculated as  
331  $(\text{Area}_{\text{diffuse+compact}} - \text{Area}_{\text{compact}}) / \text{Area}_{\text{diffuse+compact}}$ . For each animal, data was averaged  
332 from two sections per animal, with 3-4 images per section consisting of two fields from cortex,  
333 one field from dorsal subiculum and/or one field from dentate gyrus molecular layer.

334 For analysis of methoxy-X04 or ApoE colocalization within Iba1<sup>+</sup> microglia, images were  
335 collected from the costained slides described above for the 12mo female cohort of animals  
336 using confocal laser scanning microscope LSM780 (Carl Zeiss, Inc.) with Zen 2.3 SP1 software  
337 (Carl Zeiss, Inc.). 11 z-stack images at 1  $\mu\text{m}$  intervals were collected from the cortex with Plan-

338 Apochromat 20X/0.8 M27. To determine colocalization of ApoE and Iba1 staining, or methoxy-  
339 X04 and Iba1 staining, we calculated the Manders' Colocalization Coefficients (MCC) using the  
340 ImageJ plugin JACoP, as described in (Dunn et al., 2011). The same thresholds were  
341 consistently used to identify the Iba1, ApoE, or methoxy-X04 channel across animal samples.  
342 Calculations were performed on the entire z-stack of images.

343

#### 344 *A-beta peptide measurements.*

345 Frozen hippocampal tissues, described above, were homogenized in 10 volumes of TBS  
346 (50 mM Tris pH 7.5, 150 mM NaCl, including complete EDTA-free protease inhibitor cocktail  
347 (Roche) with aprotinin (20 µg/ml) and leupeptin (10 µg/ml)) in a Qiagen TissueLyser II (3 min at  
348 30 Hz). Samples were then centrifuged at 20,000 x g for 20 min at 4°C. Supernatants were  
349 collected as the "TBS fraction" and stored at -80°C until analyzed. The pellet was then  
350 homogenized in 10 volumes of 5 M guanidine HCl using the TissueLyser II and then placed on a  
351 rotisserie for 3 hours at room temperature. Samples were diluted 1:10 in a casein buffer (0.25%  
352 casein/5 mM EDTA pH 8.0 in PBS, including aprotinin (20 µg/ml) and leupeptin (10 µg/ml)),  
353 vortexed and centrifuged at 20,000 x g for 20 min at 4°C. Supernatants were collected as  
354 "GuHCl fractions". Aβ40 and Aβ42 concentrations in mouse hippocampal samples were  
355 measured using an ELISA. Briefly, rabbit polyclonal antibody specific for the C terminus of Aβ40  
356 or Aβ42 (Millipore) was coated onto plates, and biotinylated monoclonal anti-Aβ1-16 (Covance,  
357 clone 6E10) was used for detection.

358 For dot blot analyses, approximately 10 µg in 1 µl of lysate (TBS soluble fraction of  
359 homogenized mouse hippocampus) was blotted onto nitrocellulose membranes (#LC2001,  
360 Invitrogen) and incubated for at least one hour at room temperature (RT) to ensure that the blots  
361 were dry. The membrane was blocked with Blocking Buffer (MB-070, Rockland  
362 Immunochemicals Inc.) with added 0.01% Tween-20, for 1 hour at RT. The membrane was  
363 incubated with Amyloid Fibrils OC (Millipore Sigma AB2286), Oligomer A11 (Thermo Fisher  
364 Scientific AHB0052), 4G8 (Biolegend 800703) or 6E10 (Biolegend 803015) primary antibody  
365 diluted 1:1000 in Blocking Buffer for 1 hr at RT. Total protein was normalized with mouse anti-  
366 β-actin (Cell Signaling 8H10D10, 1:10000) or rabbit anti-GAPDH (Novus Biological NB300-323,  
367 1:10000). After primary antibody incubation, membranes were washed 3 times (10 minutes  
368 each) with TBST (50 mM Tris, 0.5 M NaCl, 0.01% Tween-20). The membrane was incubated  
369 with secondary antibodies in Blocking Buffer at 1:15,000 dilution (IRDye 800CW donkey anti-  
370 rabbit IgG and IRDye 680LT donkey anti-mouse IgG, LI-COR Biosciences 926-32213, 926-  
371 32212, 926-68022, and 926-68023) for 1 hour at RT. Membrane was washed 3 times (10  
372 minutes each) in TBST on rocker. Blots were scanned on Odyssey/LICOR scanner for signals  
373 followed by image analysis in Image Studio (v5.2.5, LI-COR Biosciences).

374

#### 375 *CSF collection and neurofilament light chain (NfL) analysis.*

376 A separate, mixed sex cohort of 12mo PS2APP;Trem2<sup>wt</sup> (n=8) and PS2APP;Trem2<sup>ko</sup>  
377 mice (n=8) were anesthetized and CSF was collected from the cisterna magna and placed on  
378 ice, then blood was collected from terminal cardiac puncture, placed into EDTA collection tubes  
379 and centrifuged at 20,000 x g for 2 minutes. (The two genotype groups in this analysis were not

380 littermates since we had not collected plasma or CSF from our original cohorts, and we  
381 assembled this cohort just for NfL measurements due to a recommendation received during  
382 peer review.) Plasma was collected into tubes and stored at -80°C until transfer. CSF samples  
383 were diluted 1:10 in 0.1% BSA in TBS and then stored at -80°C until transfer. Plasma and CSF  
384 samples were sent to Quanterix (Billerica, MA) for NfL measurements using the Simoa™ NF-  
385 Light Advantage Kit (product 103186). The Simoa assay is a 2-step digital immunoassay, which  
386 measures the quantity of NfL in samples using the Simoa HD-1 Analyzer and Single Molecule  
387 Array (Simoa) technology.

388

389 *Two-photon imaging of plaque and dendritic spine measurements.*

390 The somatosensory cortex from PS2APP mice carrying the Thy1:GFP-M transgene and  
391 different *Trem2* genotypes was imaged *ex vivo* via 2-photon microscopy. Single-sex cohorts  
392 used for this purpose included 6mo PS2APP females (n=7 for per *Trem2* genotype, used for  
393 both plaque counts and dendritic spine measurements) and 8mo PS2APP males (n=6 per  
394 *Trem2* genotype, used only for plaque counts). 24 hours before brain collection, animals  
395 received intraperitoneal injections of methoxy-X04 (10 mg/kg) to label amyloid structures (Klunk  
396 et al., 2002). Animals were anesthetized using isoflurane and transcardially perfused with 10  
397 ml PBS followed by 10 ml of 4% PFA + 10% sucrose in PBS, and the collected brains were  
398 fixed overnight in 4% PFA + 10% sucrose in PBS at 4°C. Postfixation, brains were mounted in  
399 agarose and immersed in PBS. Imaging and analysis were performed under blinded conditions.

400 Apical dendrites and their spines in somatosensory cortex upper layers were imaged *en*  
401 *bloc* via a two-photon laser-scanning microscope (Ultima In Vivo Multiphoton Microscopy  
402 System; Prairie Technologies) using a Ti:sapphire laser (MaiTai DeepSee Spectra Physics;  
403 Newport) tuned to 840 nm and a 60× numerical aperture 1.0 immersion objective lens  
404 (Olympus) with pixel resolution of 0.1 μm/pixel across a 1024 × 1024 pixel field of view (FOV)  
405 using 1.0 μm steps, with stack depth determined by the slant of the dendritic branch being  
406 imaged. For comparison of spine density relative to plaques in PS2APP animals, a FOV  
407 containing a dendrite and nearby plaque within 20 μm was considered “near plaque” and a FOV  
408 containing only a dendrite with no visible plaque was considered “away from plaque.” To meet  
409 the “away from plaque” criteria, we confirmed that no plaque was present in the FOV and at  
410 least 100 μm outside of the containing FOV. From each brain, at least five dendrites per  
411 condition (near plaque, away from plaque) were imaged. Dendritic spine density and size  
412 measurements were generated using custom, semiautomated image analysis routines in  
413 MATLAB (MathWorks). Spine density was estimated as the total number of visible dendritic  
414 spines divided by the corresponding length of dendrite. Relative spine volumes were estimated  
415 for each detected spine based on the number of corresponding GFP<sup>+</sup> pixels in x, y, z  
416 dimensions above a local threshold applied as part of an automated image segmentation  
417 algorithm. For *en bloc* plaque measurements, larger volume stacks were collected using a 20×  
418 immersion objective lens across a 1024 × 1024 pixel FOV with 2 μm steps (~200 μm depth).  
419 Plaque density was quantified by a threshold-based MATLAB routine designed to automatically  
420 identify methoxy-X04-labeled plaques.

421

422 *Statistical analysis*

423 All values are expressed as mean  $\pm$  SEM. Statistical analysis was performed using the  
424 JMP (v14.2, SAS Institute) or Prism (v8.3.0 for Mac, GraphPad) software packages. To  
425 compare differences between PS2APP;Trem2<sup>wt</sup> and PS2APP;Trem2<sup>ko</sup> groups we performed  
426 unpaired t-tests. For comparisons of three or more groups we performed one-way ANOVA  
427 followed by Tukey's multiple comparisons test. The 6-7mo cohort of male and female mice were  
428 purposely analyzed separately to determine the effects of *Trem2* deficiency in each sex since  
429 female mice have accelerated amyloid pathology compared to males, and we did not want an  
430 analysis of interactions between sex and *Trem2* genotype to be confounded by the age-  
431 dependent differences in pathology between males and females.

432

433

434 **RESULTS**

435

436 *Plaque-associated microgliosis is impaired in PS2APP;Trem2<sup>ko</sup> microglia*

437

438 PS2APP mice express transgenes encoding familial AD mutations in human presenilin  
439 2 (PS2 N141I) and amyloid precursor protein (APP K670N/M671L). By 4 months of age  
440 the first deposits of  $\beta$ -amyloid plaque are detected, with age-dependent plaque  
441 accumulation occurring faster in females than in males (Kallop et al., 2014; Ozmen et al.,  
442 2009). To determine the role of *Trem2* in the progression of amyloid disease pathology,  
443 we crossed PS2APP mice with *Trem2*-deficient mice and examined plaque-related  
444 phenotypes in single-sex groups at various stages of pathology. We found a stark  
445 reduction in Iba1<sup>+</sup> microglial clusters in PS2APP;Trem2<sup>ko</sup> mice at 4, 6-7, 12, and 19-22  
446 months compared to PS2APP;Trem2<sup>wt</sup> (Fig. 1A,B). In addition, PS2APP;Trem2<sup>ko</sup> brains  
447 showed reduced staining for CD68 marking active microglial lysosomes by IHC (Fig.  
448 1C,D), reduced percentage of CD45<sup>high</sup> ("activated") microglia by flow cytometry (Fig.  
449 1E,F), and reduced percentage of methoxy-X04<sup>+</sup> (amyloid-containing) microglia by flow  
450 cytometry (Fig. 1G,H). Analysis of confocal z-stack images of cortical tissue from 12-  
451 month (12mo) animals also found a significant reduction in the fraction of Iba1 and  
452 methoxy-X04 signals that colocalized with each other (Fig. 1-1). We also observed  
453 reductions in total Iba1 and Gfap staining at the later ages, indicative of reduced extents  
454 of microgliosis and astrogliosis, respectively, in PS2APP;Trem2<sup>ko</sup> mice (Fig. 1-1). These  
455 observations were consistent with reports of *Trem2* deletion in other  $\beta$ -amyloidosis

456 models (Jay et al., 2015; Parhizkar et al., 2019; Wang et al., 2015; Wang et al., 2016;  
457 Yuan et al., 2016) and suggested that *Trem2* deficiency impairs the ability of microglia  
458 to engage plaques and phagocytose A $\beta$  filbrils/aggregates.

459

460 *Trem2*-dependent induction of the Proliferation and Neurodegeneration-related gene  
461 expression modules

462

463 To further characterize the attenuated microglial response to  $\beta$ -amyloid pathology in  
464 PS2APP;*Trem2*<sup>ko</sup> mice, we FACS-isolated the resident myeloid cell population from the  
465 cortex+hippocampus of 14-15mo PS2APP;*Trem2*<sup>wt</sup> vs. PS2APP;*Trem2*<sup>ko</sup> mice and  
466 compared their transcriptomic profiles by RNA sequencing (raw RNA-Seq data  
467 deposited in NCBI GEO under accession number GSE140744). Although not affording  
468 single cell resolution, our approach provided certain overall advantages—genome-wide  
469 analysis, robust detection of low-copy transcripts, and avoidance of artifactual gene  
470 expression that occurs during warm-temperature dissociations—compared to other  
471 approaches for transcription profiling of *Trem2*<sup>ko</sup> microglia in  $\beta$ -amyloid models that used  
472 different cell isolation techniques and/or different RNA detection methods such as  
473 microarray, Nanostring, or single-cell RNAseq (Griciuc et al., 2019; Keren-Shaul et al.,  
474 2017; Krasemann et al., 2017; Wang et al., 2015).

475

476 Applying cutoffs of  $\geq 2$ -fold change and adjusted p-value  $\leq 0.05$ , we observed only 7  
477 transcripts with increased abundance in PS2APP;*Trem2*<sup>ko</sup> vs. PS2APP;*Trem2*<sup>wt</sup>  
478 microglia (excluding *Trem1*, an artifact of the knockout cassette insertion (Kang et al.,  
479 2018)). In contrast, 144 transcripts (excluding *Trem2*) showed reduced abundance in  
480 PS2APP;*Trem2*<sup>ko</sup> compared to PS2APP;*Trem2*<sup>wt</sup> microglia using the same cutoffs (Fig.  
481 2A; see Fig. 2-1 extended data table of genome-wide expression values for each  
482 sample and summary statistics for differential gene expression). The majority of these  
483 transcripts showed upregulation in microglial expression profiles from the PS2APP  
484 model (Friedman et al., 2018) and other models of  $\beta$ -amyloid pathology (Orre et al.,  
485 2014; Wang et al., 2015) compared to non-transgenic mice (Fig. 2A). Therefore, their  
486 reduced expression in PS2APP;*Trem2*<sup>ko</sup> microglia is another manifestation of the

487 impaired microglial response to  $\beta$ -amyloid pathology. The dependence of these  
488 transcripts on Trem2 for their induction in PS2APP microglia was roughly concordant  
489 with published data from sorted microglial populations from the 5xFAD model (Wang et  
490 al., 2015) (Fig. 2A).

491

492 Four of the eight most starkly reduced transcripts (in terms of fold change) in  
493 PS2APP;Trem2<sup>ko</sup> microglia are regulators of canonical Wnt signaling or proliferation—  
494 *Dkk2*, *Wif1*, *Ctnna3*, and *Asb11* (Fig. 2B). *Dkk2*, *Wif1*, and *Ctnna3* can all negatively  
495 regulate Wnt activity (Busby et al., 2004; Gage et al., 2008; Hsieh et al., 1999), while  
496 *Asb11* is important for maintaining progenitor cell activity in multiple cell types (Diks et  
497 al., 2006; Tee et al., 2012). Although the lack of induction for negative Wnt regulators  
498 might suggest that Wnt-related signaling was enhanced in Trem2<sup>ko</sup> microglia, another  
499 possibility is that Wnt-related signaling was impaired since *Dkk2* is also a context-  
500 dependent activator of the pathway (Devotta et al., 2018; Mao and Niehrs, 2003; Wu et  
501 al., 2000) and since induction of regulators including *Wif1* can occur downstream of  
502 active  $\beta$ -catenin as negative feedback (Boerboom et al., 2006; Diep et al., 2004).  
503 Supporting this interpretation, the Gene Ontology (GO) knowledgebase identified  
504 “positive regulation of canonical Wnt signaling pathway” as a biological process  
505 overrepresented (fold-enrichment = 10.3, FDR = 0.026) among the 144 transcripts  
506 transcripts with  $\geq 2$ -fold reduced abundance in PS2APP;Trem2<sup>ko</sup> microglia (Fig. 2-2A),  
507 with six positive factors in Wnt signaling showing reduced expression including *Fzd9*  
508 (Karasawa et al., 2002), *Sulf2* (Lai et al., 2010), *Bambi* (Lin et al., 2008), *Ptk7* (Berger et  
509 al., 2017), and *Aspm* (Buchman et al., 2011) along with *Dkk2* (Fig. 2C). We also  
510 analyzed recently published microglia RNA-Seq expression profiles from the 5xFAD  
511 model (Griciuc et al., 2019) and observed similar Trem2-dependent induction for the  
512 nine above-mentioned genes, with the exception of *Ptk7* (Figure 2-2B). The reduced  
513 expression of Wnt-related signaling components and regulators in PS2APP;Trem2<sup>ko</sup>  
514 microglia may be consistent with previous reports of coordinated signaling between  
515 Trem2 and  $\beta$ -catenin pathways within microglia (Zheng et al., 2017; Zulfiqar and  
516 Tanriover, 2017).

517

518 Other GO biological processes implicated as being downregulated in PS2APP;Trem2<sup>ko</sup>  
519 microglia included positive regulation of bone resorption (fold-enrichment=24.6,  
520 FDR=0.030), protein kinase B signaling (fold-enrichment=16.2, FDR=0.047), negative  
521 regulation of tumor necrosis factor production (fold-enrichment=14.1, FDR=0.026),  
522 positive regulation of smooth muscle cell migration (fold-enrichment=13.9, FDR=0.025),  
523 transmembrane receptor protein tyrosine kinase signaling pathway (fold-enrichment=5.9,  
524 FDR=0.0037), and actin cytoskeleton reorganization (fold-enrichment=3.9, FDR=0.044)  
525 (Fig. 2-2A). The Trem2-dependent genes identified in these processes may underlie  
526 described roles for Trem2 in osteoclast function (Cella et al., 2003; Paloneva et al.,  
527 2003), AKT and mTOR signaling (Ulland et al., 2017), attenuation of pro-inflammatory  
528 macrophage activation (Turnbull et al., 2006), chemotaxis (Mazaheri et al., 2017), and  
529 DAP12 signaling (Bouchon et al., 2001).

530

531 We recently defined a number of gene expression modules that can be used to  
532 characterize the diverse ways that microglia respond to environmental and genetic  
533 perturbations (Friedman et al., 2018). In PS2APP compared to non-transgenic microglia,  
534 several of these gene sets were upregulated including the Neurodegeneration-related,  
535 Interferon-related, Proliferation, and LPS-related modules, while the Microglia and Brain  
536 Myeloid modules that typify microglia in their “homeostatic” or “resting” state were  
537 modestly but significantly downregulated (Fig. 2D, Fig. 2-3). (The entirety of these  
538 changes is roughly equivalent to the so-called DAM (Keren-Shaul et al., 2017) or MgND  
539 (Krasemann et al., 2017) microglial activation profiles.) These findings underscore the  
540 utility of these gene modules in characterizing microglial activation states. For instance,  
541 even though only 5 of 82 genes in the Proliferation module were upregulated strongly  
542 enough in PS2APP microglia to reach genome-wide significance (adj.  $p \leq 0.05$ ), the  
543 overall expression of the module was clearly enriched compared to microglia from non-  
544 transgenic mice (Fig. 2D, Fig. 2-3).

545

546 We next analyzed the degree to which these modular changes in microglial gene  
547 expression in PS2APP mice depended on Trem2. Again, despite only 2 of 82 genes  
548 (*Ccna2* and *Aspm*) showing significant reduction in transcript abundance after

549 correction for genome-wide analysis, the overall induction of the Proliferation module  
550 was compromised in PS2APP;Trem2<sup>ko</sup> microglia (Fig. 2D, Fig. 2-3). We also observed  
551 less induction of the Proliferation module in Trem2<sup>ko</sup> microglia expression profiles from  
552 the 5xFAD model (Griciuc et al., 2019) (Fig. 2-2C). The reduced expression of  
553 proliferation-related genes was consistent with the notion mentioned above that Wnt-  
554 related signaling was impaired and also corroborated reports from other  $\beta$ -amyloid  
555 models that proliferation markers such as Ki67 or BrdU were observed less frequently in  
556 *Trem2*-deficient microglia (Jay et al., 2017a; Wang et al., 2016).

557

558 As expected, the Neurodegeneration-related gene set—which overlaps with the so-  
559 called DAM (Keren-Shaul et al., 2017) and MGnD (Krasemann et al., 2017) genes but  
560 relates more specifically to neurodegenerative disease models—was notably impaired  
561 in PS2APP;Trem2<sup>ko</sup> microglia (Fig. 2D, Fig. 2-3). Of the 134 genes in this set, 80  
562 showed upregulation in PS2APP vs. normal microglia (Friedman et al., 2018), and  
563 roughly half of these showed impaired induction in PS2APP;Trem2<sup>ko</sup> microglia (adjusted  
564 p-values  $\leq 0.05$ ) (Fig. 2E). Unlike the clear requirement of Trem2 for induction of many  
565 genes in the Neurodegeneration-related gene set, the downregulation of the Microglia  
566 and Brain Myeloid modules that normally occurs during any CNS challenge (Friedman  
567 et al., 2018) was not prevented by *Trem2* deletion since expression of these modules  
568 was similar in PS2APP;Trem2<sup>wt</sup> and PS2APP;Trem2<sup>ko</sup> microglia (Fig. 2D, Fig. 2-3). No  
569 effect of *Trem2* deletion on the induction of the LPS-related and Interferon-related  
570 modules was observed. Overall, our results are similar to previous analysis of the  
571 5xFAD model, in which the microglial induction of many DAM genes showed substantial  
572 Trem2 dependence while the downregulation of so-called microglial “homeostatic”  
573 genes appeared largely Trem2-independent (Keren-Shaul et al., 2017).

574

575 *Plaque load is reduced in aged PS2APP;Trem2<sup>ko</sup> mice*

576

577 In the 5xFAD mouse model, plaque load was reportedly unchanged in 4mo Trem2<sup>ko</sup>  
578 mice but increased in 8mo Trem2<sup>ko</sup> hippocampus (Wang et al., 2015; Wang et al., 2016;  
579 Yuan et al., 2016). In the APPPS1 model, plaque load was reduced in Trem2<sup>ko</sup> brains at

580 2mo, reduced or unchanged at 4mo, and increased in the cortex at 8mo (Jay et al.,  
581 2017a; Jay et al., 2015).

582

583 The reductions in microglial clustering and amyloid engulfment in PS2APP;Trem2<sup>ko</sup>  
584 mice (Fig. 1) suggested that more plaque might accumulate over time in these brains,  
585 relative to PS2APP;Trem2<sup>wt</sup> mice. Indeed, using the Campbell-Switzer silver stain to  
586 label amyloid plaque (Campbell et al., 1987; Switzer, 2000), we observed that plaque  
587 burden was increased in 6-7mo PS2APP;Trem2<sup>ko</sup> females, and trending upward but not  
588 reaching significance in 6-7mo PS2APP;Trem2<sup>ko</sup> males (Fig. 3A,B). We observed  
589 similar results in distinct cohorts of 6mo females and 8mo males by in vivo labeling of  
590 plaque using methoxy-X04 injection, followed by fixation and two-photon imaging of  
591 intact somatosensory cortex (Fig. 3-1). We did not observe any effect of *Trem2* deletion  
592 on the low levels of plaque deposition detected at the earliest stage examined (4mo).

593

594 We expected to see further exacerbation of amyloid plaque load in *Trem2*-deficient  
595 brains at more advanced ages, but, to our surprise, plaque load was reduced in 12mo  
596 PS2APP;Trem2<sup>ko</sup> females and in 19-22mo PS2APP;Trem2<sup>ko</sup> males compared to  
597 PS2APP;Trem2<sup>wt</sup> mice (Fig. 3A,B). An intermediate reduction in plaque load was  
598 observed in *Trem2* heterozygous (PS2APP;Trem2<sup>het</sup>) mice at 19-22mo (the only age  
599 where heterozygous mice were analyzed) (Fig 3A). At this age, the Campbell-Switzer  
600 stain also revealed a distinctive pattern of “amber core” amyloid staining in PS2APP  
601 brains (Fig. 3C), thought to represent a mature form of highly condensed plaque. These  
602 amber cores were reduced in PS2APP;Trem2<sup>het</sup> and nearly absent in PS2APP;Trem2<sup>ko</sup>  
603 brains, indicating that Trem2-dependent microglial activity is essential for the formation  
604 of these particular amyloid structures.

605

606 Overall, our results are reminiscent of a recent study of APPPS1 mice which showed  
607 that *Trem2* deletion produced increased seeding of amyloid plaques at early ages but  
608 slower rates of amyloid plaque accumulation at later ages (Parhizkar et al., 2019).

609

610 *Reduced plaque consolidation, elevated neurotoxic A $\beta$  species, and ApoE-laden*  
611 *microglia in Trem2-deficient brains*

612

613 In contrast to the effects of *Trem2* deletion on total plaque burden that varied with age  
614 or sex, we observed consistent changes in plaque compaction and composition across  
615 ages and sexes. We used the X-34 stain and confocal microscopy to visualize plaque  
616 morphology. Although we were blinded to *Trem2* genotype, there was an obvious  
617 difference in plaque appearance between PS2APP;*Trem2*<sup>wt</sup> and PS2APP;*Trem2*<sup>ko</sup>  
618 brains, with X-34<sup>+</sup> structures in PS2APP;*Trem2*<sup>ko</sup> brains looking more splayed and less  
619 compact (Fig. 4A), similar to descriptions of Trem2-dependent plaque alterations in  
620 other  $\beta$ -amyloid models (Wang et al., 2016; Yuan et al., 2016). Using an algorithm  
621 based on X-34 signal intensity to quantify the degree of plaque diffuseness, we  
622 observed that plaque morphologies were significantly more diffuse in PS2APP;*Trem2*<sup>ko</sup>  
623 brains in both sexes at all ages tested (Fig. 4B).

624

625 Because stains such as Campbell-Switzer, methoxy-X04, and X-34 only label fibrillar  
626 amyloid structures, we also measured the total abundance of A $\beta$ 40 and A $\beta$ 42 peptides  
627 in soluble (TBS) and insoluble (GuHCl) hippocampal fractions by ELISA. The  
628 abundance of A $\beta$  peptides rose markedly with age while the A $\beta$ 42:A $\beta$ 40 ratio declined,  
629 particularly in the GuHCl fraction (Fig. 5). Notably, the A $\beta$ 42:A $\beta$ 40 ratio was higher in  
630 PS2APP;*Trem2*<sup>ko</sup> than in PS2APP;*Trem2*<sup>wt</sup> brains, in both TBS and GuHCl fractions  
631 across ages (Fig. 5A,B). The elevated A $\beta$ 42:A $\beta$ 40 ratio in PS2APP;*Trem2*<sup>ko</sup> brains  
632 resulted more from reduced abundance of A $\beta$ 40 than from increased abundance of  
633 A $\beta$ 42 (Fig. 5-1), although A $\beta$ 42 abundance was elevated in the 6-7mo females,  
634 coinciding with the increased plaque deposition we observed in that group (Fig. 3A).  
635 Together with our observation that total amyloid plaque is reduced in PS2APP;*Trem2*<sup>ko</sup>  
636 brains at later ages (Fig. 3A), these results suggest that the elevated A $\beta$ 42:A $\beta$ 40 ratio in  
637 *Trem2*-deficient brains may increase plaque seeding at younger ages (since A $\beta$ 42 is  
638 more prone to aggregate and deposit than A $\beta$ 40 (Klein, 2002)) while reducing the  
639 incorporation and compaction of A $\beta$  into existing plaques at older ages (since A $\beta$ 40

640 permeates dense core structures more readily than A $\beta$ 42 (Condello et al., 2015)). Thus,  
641 Trem2 may both restrict the initial seeding of plaques and promote sequestration and  
642 compaction of A $\beta$  into existing plaques.

643

644 To determine if the elevated A $\beta$ 42:A $\beta$ 40 ratio was accompanied by altered abundance  
645 of soluble, fibrillar A $\beta$  oligomers, we performed non-denaturing dot blots of hippocampal  
646 TBS homogenate supernatants from 12mo females. Using the conformation-specific OC  
647 antibody (Tomic et al., 2009), we detected significantly higher levels of soluble fibrillar  
648 A $\beta$  oligomers in the soluble fraction from PS2APP;Trem2<sup>ko</sup> mice (Fig. 5C,D), and we  
649 observed a positive correlation between the amount of OC<sup>+</sup> fibrillar oligomers in this  
650 fraction and the A $\beta$ 42:A $\beta$ 40 ratio (Fig. 5E). In contrast, when we used the pan-reactive  
651 6E10 A $\beta$  antibody to detect total A $\beta$  species in this fraction, the abundance trended  
652 slightly downward in PS2APP;Trem2<sup>ko</sup> mice and correlated negatively with A $\beta$ 42:A $\beta$ 40  
653 ratio (Fig. 5F-H). Similar respective trends were also seen when staining with the  
654 prefibrillar A $\beta$  oligomer antibody A11 and pan-reactive 4G8 A $\beta$  antibody (data not  
655 shown). As a control, we spotted hippocampal TBS homogenate supernatant from a  
656 PS2APP;Bace1<sup>ko</sup> animal (Meilandt et al., 2019)—in which soluble APP is still produced  
657 by  $\alpha$ -cleavage while  $\beta$ -cleavage and thus A $\beta$  production are prevented—and  
658 demonstrated that the OC antibody had minimal detection whereas 6E10 still had  
659 substantial signal (compare # symbols in Fig. 5C,F and dotted lines in Fig. 5D,G from a  
660 PS2APP;Bace1<sup>ko</sup> mouse), consistent with the ability of 6E10 to detect both soluble APP  
661 and A $\beta$  peptides. These results suggest that in the absence of Trem2 the increased  
662 A $\beta$ 42:A $\beta$ 40 ratio enhances the potential shift of soluble A $\beta$  to a fibrillar oligomeric form.  
663 Alternatively, the increased abundance of fibrillar A $\beta$  oligomers in the TBS-soluble  
664 fraction could result from reduced incorporation into highly condensed plaques in brains  
665 with *Trem2*-deficient microglia.

666

667 *ApoE* is one of the most highly induced genes in mouse microglia in response to  
668 neurodegenerative stimuli (Deczkowska et al., 2018). A recent report in the APPPS1  
669 model found that plaque-associated ApoE was reduced in *Trem2*-deficient mice

670 (Parhizkar et al., 2019). To learn whether *Trem2* deletion altered ApoE localization in  
671 the PS2APP model and whether such alteration correlated with observed changes in  
672 plaque abundance, morphology, or composition, we co-stained for ApoE, plaques  
673 (methoxy-X04), and microglia (Iba1). In contrast to the findings of Parhizkar et al.,  
674 quantification of plaque-associated ApoE in whole brain sections found a significant  
675 increase in female PS2APP;*Trem2*<sup>ko</sup> mice at 6-7mo and 12mo ages, but no significant  
676 changes in male cohorts at any age tested (Fig. 6A). The ApoE immunostaining pattern  
677 was especially prominent in, but not limited to, the hippocampal subiculum where  
678 plaque tends to first deposit (Fig. 6B). While the incongruous results between studies  
679 may be explained by differences between mouse models, other variations in sampling  
680 and technical procedures could also account for the differences. Parhizkar et al.  
681 examined 4mo males; we only examined females at that age, and our findings of  
682 elevated plaque-associated ApoE in *Trem2*-deficient females were only observed at  
683 older ages. The studies used different ApoE monoclonal antibodies that likely interact  
684 with distinct epitopes or configurations of ApoE (Kim et al., 2012) and whose binding  
685 may be differentially impacted by variations in staining procedure. We immunostained  
686 for ApoE first, followed by plaque labeling which involves treatments with ethanol and  
687 NaOH. Parhizkar et al. did the plaque labeling first, followed by the ApoE immunostains,  
688 so the nature of the ApoE at the time of immunostaining was somewhat different  
689 between studies.

690

691 Parhizkar et al. also reported that colocalization of ApoE with Iba1<sup>+</sup> microglia was  
692 reduced in *Trem2*-deficient mice. To assess this finding in the PS2APP model, we  
693 performed confocal imaging on the ApoE/Iba1/methoxy-X04 costains from the cortex of  
694 12mo females and again observed a contrasting result. Instead of ApoE labeling being  
695 diminished, we observed microglia in PS2APP;*Trem2*<sup>ko</sup> mice to be markedly laden with  
696 ApoE (Fig. 6C,D), suggesting that *Trem2*-deficient microglia exhibit deficits in lipid  
697 clearance. At the mRNA level, we did not detect a difference in *ApoE* expression  
698 between PS2APP;*Trem2*<sup>wt</sup> and PS2APP;*Trem2*<sup>ko</sup> microglia (Fig. 6E; see also Fig. 2E).  
699 Although two groups have reported reductions in microglial *ApoE* expression in the  
700 APPS1 model when *Trem2* is deleted (Krasemann et al., 2017; Parhizkar et al., 2019),

701 this does not appear to be a typical feature of *Trem2* deficiency in  $\beta$ -amyloidosis models  
702 since previous analyses in the 5xFAD model observed *Trem2*-independent *ApoE*  
703 induction in either bulk microglia microarray (Fig. 6F) (Wang et al., 2015) or single cell  
704 microglia RNA-Seq profiles (Keren-Shaul et al., 2017). In a very recent dataset of bulk  
705 microglia RNA-Seq profiles from 5xFAD mice (Griciuc et al., 2019), we did see a 2-fold  
706 decrease in the extent of *ApoE* induction in *Trem2*-deficient microglia, but the gene was  
707 still highly induced relative to the expression level in microglia from non-transgenic mice  
708 (Fig. 6F). Altogether, our evidence indicates that microglial *ApoE* expression is induced  
709 by A $\beta$ -driven neuropathology in a largely *Trem2*-independent manner, and that *Trem2*-  
710 deficient microglia accumulate disproportionately large amounts of ApoE compared to  
711 the smaller ApoE puncta observed in normal PS2APP microglia (Fig. 6C).

712

713 *Axonal dystrophy, dendritic spine loss, and CSF NfL detection are exacerbated in*  
714 *PS2APP;*Trem2*<sup>ko</sup> mice*

715

716 The elevated A $\beta$ 42:A $\beta$ 40 ratio and fibrillar A $\beta$  oligomers in PS2APP;*Trem2*<sup>ko</sup> brains  
717 would seem to be detrimental for neuronal health since A $\beta$ 42 oligomers are commonly  
718 understood to be the more toxic form of A $\beta$  (Haass and Selkoe, 2007; Klein, 2002).  
719 Alternatively, the reduced plaque load in aged *Trem2*<sup>ko</sup> brains suggested a possible  
720 benefit of *Trem2* deficiency. Therefore, we turned to measures of neuronal dystrophy to  
721 better understand the potential consequences of loss of *Trem2* function.

722

723 First, we looked at neuritic dystrophy around plaque (D'Amore et al., 2003) by  
724 fluorescent co-staining using methoxy-X04 to label plaque, anti-Iba1 to label microglia,  
725 and anti-Lamp1 to label dystrophic axons (Gowrishankar et al., 2015) (Fig. 7A). The  
726 methoxy-X04/Iba1 costain showed that microglial association with plaque was severely  
727 compromised in PS2APP;*Trem2*<sup>ko</sup> brains at all examined ages (Fig. 7A,B),  
728 corroborating our earlier Iba1 immunohistochemical stains that measured microglial  
729 clustering. The Lamp1 immunolabeling, which stains dilated dystrophic axons, revealed  
730 two important findings. First, on a per plaque basis, axonal dystrophy was exacerbated  
731 from 7 months onward in PS2APP;*Trem2*<sup>ko</sup> mice (Fig. 7C), similar to findings in other  $\beta$ -

732 amyloid models (Wang et al., 2016; Yuan et al., 2016). This is consistent with the idea  
733 that the diffuse plaque structures and elevated A $\beta$ 42:A $\beta$ 40 ratio in Trem2<sup>ko</sup> brains are  
734 more damaging to surrounding axons than the more compacted, A $\beta$ 40-enriched  
735 plaques in PS2APP;Trem2<sup>wt</sup> brains. Second, the total Lamp1<sup>+</sup> area was also increased  
736 from 7 months onward in PS2APP;Trem2<sup>ko</sup> brain sections (Fig. 7D), indicating that total  
737 axonal damage was exacerbated at later ages despite the reduced plaque burden.  
738 These data strongly suggest that the Trem2-dependent clustering of microglia and their  
739 functions around plaque serve to mitigate the neurotoxic effects of A $\beta$ .

740

741 Another method we used to visualize neuronal pathology was an amino-cupric-silver  
742 stain or “disintegrative degeneration” stain that labels damaged or degenerating  
743 neurons (de Olmos et al., 1994; Switzer, 2000). Overall, the staining pattern appeared  
744 very similar to the Lamp1 stain, with “bouquets” of argyrophilic structures presumably  
745 surrounding plaques throughout the cortex and hippocampus. Staining was also  
746 observed in relevant white matter tracts such as the corpus callosum, perforant path  
747 and fornix, suggesting that degenerating axonal processes are not restricted to  
748 dystrophic neurites around plaques. Degenerating neurites detected by this stain were  
749 more abundant in PS2APP;Trem2<sup>ko</sup> brains of the 12mo female and 19-22mo male  
750 cohorts (Fig. 8A,B). Thus, again, axonal damage was exacerbated in Trem2-deficient  
751 mice from older ages despite the fact that plaque accumulation was reduced. The  
752 intermediate effect of Trem2 heterozygosity on microglial clustering around plaque (Figs.  
753 1A and 7B) and Campbell-Switzer plaque staining (Fig. 3A) but not on plaque  
754 diffuseness (Fig. 4B), A $\beta$ 42:A $\beta$ 40 ratio (Fig. 5A), or neuritic dystrophy (Figs. 7C,D and  
755 8A) suggested that the form rather than the amount of plaque correlates with neuronal  
756 damage, and that sufficient microgliosis occurs in PS2APP;Trem2<sup>het</sup> mice to enable  
757 plaque compaction and neuroprotection.

758

759 Neurofilament light chain (NfL) measured in the cerebrospinal fluid (CSF) or plasma has  
760 recently emerged as a potential biomarker of neurodegeneration in human patients and  
761 in mouse disease models (Bacioglu et al., 2016; Khalil et al., 2018). To determine  
762 whether Trem2 deficiency altered NfL levels, we collected plasma and CSF from a

763 separate, mixed sex cohort of 12mo PS2APP;Trem2<sup>wt</sup> and PS2APP;Trem2<sup>ko</sup> mice.  
764 PS2APP;Trem2<sup>ko</sup> mice had significantly greater NfL levels in the CSF compared to  
765 PS2APP;Trem2<sup>wt</sup> mice (Fig. 8C), consistent with the measures of increased axonal  
766 dystrophy that were observed by histopathology in *Trem2*-deficient females at this age.  
767 Perhaps surprisingly, we did not observe a difference in plasma NfL levels between  
768 genotypes (Fig. 8C), suggesting that CSF NfL measurements better represent ongoing  
769 neuronal damage or degeneration in the CNS than plasma measurements.

770

771 Finally, we looked at whether another feature of neuronal pathology observed in AD  
772 tissues and  $\beta$ -amyloid mouse models—reduced synaptic density, particularly near  
773 plaque (Spires and Hyman, 2004; Spires et al., 2005; Tsai et al., 2004)—was altered in  
774 *Trem2*-deficient mice. In  $\beta$ -amyloid models, the reduction in synapse number requires  
775 the presence of microglia since depleting the microglial cell population largely prevents  
776 loss of synaptic density (Olmos-Alonso et al., 2016; Spangenberg et al., 2016).  
777 Therefore, we asked whether *Trem2* deletion and the resulting lack of activated, plaque-  
778 associated microglia would prevent the dendritic spine loss from occurring or would  
779 worsen it. To answer this, we crossed the Thy1:GFP-M line, which labels a sparse  
780 population of excitatory neurons, into the PS2APP model and analyzed a cohort of 6mo  
781 female mice with different *Trem2* genotypes. Spine density loss in the proximity of  
782 plaques was not rescued by *Trem2* deletion, but was actually further exacerbated in  
783 PS2APP;Trem2<sup>ko</sup> mice compared to PS2APP;Trem2<sup>wt</sup> or PS2APP;Trem2<sup>het</sup> groups (Fig.  
784 9). Thus, Trem2 is not required for microglia-mediated dendritic spine loss around  
785 plaque and in fact Trem2 seems to hedge against synapse loss. Overall, the  
786 exacerbated axonal dystrophy and dendritic spine loss observed around plaque in  
787 PS2APP;Trem2<sup>ko</sup> mice imply that Trem2-dependent microglial activity is fundamentally  
788 neuroprotective in  $\beta$ -amyloid-driven models of AD-like pathology.

789

790

791 **DISCUSSION**

792

793 In this study we examined the role of Trem2 in microglial activation, plaque  
794 accumulation, and neuronal dystrophy in the PS2APP model of  $\beta$ -amyloidosis. We  
795 observed both age- and sex-dependent effects of *Trem2* deletion on plaque abundance  
796 assessed using the Campbell-Switzer silver stain, with slightly more plaque in  
797 PS2APP;*Trem2*<sup>ko</sup> females at the 6-7mo age but markedly less plaque in both female  
798 and male PS2APP;*Trem2*<sup>ko</sup> mice at later ages. Together with a recent similar report  
799 (Parhizkar et al., 2019), these results suggest that Trem2-dependent microglial activity  
800 may both restrain the formation/seeding of plaques at an early stage of pathology—  
801 conceivably through uptake and degradation of soluble A $\beta$  species—but also enhance  
802 the sequestration of A $\beta$  into existing plaque structures, particularly at later stages of  
803 pathology.

804  
805 At all ages examined, and in both sexes, microglial clustering around plaque and other  
806 measurements of microglial activation were sharply reduced in PS2APP;*Trem2*<sup>ko</sup> mice.  
807 Transcriptional induction of the Neurodegeneration-related modules, the Proliferation  
808 module, and certain genes related to Wnt regulation was impaired in PS2APP;*Trem2*<sup>ko</sup>  
809 microglia. Presumably as a consequence of the impaired microglial response around  
810 plaque, plaques in PS2APP;*Trem2*<sup>ko</sup> brains displayed a more diffuse morphology than  
811 in PS2APP;*Trem2*<sup>wt</sup> brains. From 6-7mo onward, axonal injury was magnified in  
812 PS2APP;*Trem2*<sup>ko</sup> mice, even at later ages when the abundance of argyrophilic amyloid  
813 plaques was diminished. Our finding that plaque-proximal dendritic spine loss was  
814 exacerbated in PS2APP;*Trem2*<sup>ko</sup> mice further underscored that the Trem2-dependent  
815 microglial activation around plaque is protective for neurons and is distinct from  
816 microglia-mediated, complement-mediated activities that contribute to synapse loss in  
817  $\beta$ -amyloid models (Fonseca et al., 2004; Hong et al., 2016; Shi et al., 2017; Wu et al.,  
818 2019). It will be important for future studies of microglial modulation in mouse models to  
819 analyze plaque-associated neuritic dystrophy and not assume that decreases (or  
820 increases) in amyloid plaque burden are evidence of beneficial (or detrimental) effects.

821  
822 While the elevated A $\beta$ <sub>42</sub>:A $\beta$ <sub>40</sub> ratio we observed in the soluble fraction of  
823 PS2APP;*Trem2*<sup>ko</sup> brains could reflect direct deficits in the Trem2-mediated binding and

824 clearance of oligomeric A $\beta$ 42 by microglia (Lessard et al., 2018; Yeh et al., 2016; Zhao  
825 et al., 2018), it could also reflect enhanced clearance of A $\beta$ 40 through other means  
826 such as vascular efflux. The resulting elevation in soluble A $\beta$ 42:A $\beta$ 40 ratio may give rise  
827 to the increased plaque formation we observed in 6-7mo females, similar to the  
828 increased plaque seeding activity observed by others at a similar age in another model  
829 when *Trem2* was deleted (Parhizkar et al., 2019). Given that A $\beta$ 40 is more easily  
830 incorporated into existing dense plaque structures than A $\beta$ 42 (Condello et al., 2015),  
831 our observation that the A $\beta$ 42:A $\beta$ 40 ratio declines as the mice age, particularly in the  
832 insoluble fraction, is consistent with the accumulation of compact plaques in size and  
833 number over time in the brains of PS2APP mice. The reduction of this plaque  
834 accumulation activity in PS2APP;*Trem2*<sup>ko</sup> brains may underlie the elevated levels of  
835 fibrillar oligomeric A $\beta$  we detected in the soluble fraction, which may in turn be a source  
836 of increased neuronal injury in these animals.

837

838 The weakness of correlation between plaque abundance and cognitive status in  
839 humans, along with several unsuccessful clinical trials aimed at preventing cognitive  
840 decline by reducing brain A $\beta$  levels, has led some to question the relevance of A $\beta$  in the  
841 etiology and progression of AD (Itzhaki et al., 2016; Krstic and Knuesel, 2013; Morris et  
842 al., 2014). Moreover, many have proposed that chronic microglial activation is a key  
843 damaging agent that contributes to the neurotoxic environment in AD (Heneka et al.,  
844 2015; Park et al., 2018). Our results suggest the opposite, since preventing the  
845 microglial response to A $\beta$  pathology via *Trem2* deletion reversed neither axonal  
846 dystrophy nor dendritic spine loss around plaque and in fact made both of these  
847 pathologies worse. *Trem2* deletion also increased the amount of NfL detected in CSF.  
848 Evidence in humans and mice supports the mechanistic model that  $\beta$ -amyloid pathology  
849 accelerates the accumulation of tau pathology or enhances its spreading (He et al.,  
850 2018; Jack et al., 2018; Jacobs et al., 2018; Pooler et al., 2015), and a new report  
851 indicates that this effect is further magnified in *Trem2*-deficient mice (Leyns et al., 2019).  
852 Altogether, these findings suggest that the form of microglial activation brought on by

853 A $\beta$ -related pathologies (the DAM state, or at least the Trem2-dependent component of  
854 it) protects neurons by limiting A $\beta$ -induced neuronal injury.

855

856 Supporting the notion that microglial activation is primarily beneficial in the context of  
857 AD pathology, elevated PET signal for ligands of the “neuroinflammation marker” TSPO  
858 have predicted better cognitive measures and slower AD progression in mice with  $\beta$ -  
859 amyloid pathology and human patients, respectively (Focke et al., 2019; Hamelin et al.,  
860 2016). The fact that plaques in Trem2-deficient mice are more injurious to adjacent  
861 neurites but show weaker labeling with molecular probes (Thioflavin S, methoxy-X04  
862 and X-34) related to those used in the clinic ( $^{11}\text{C}$ -PiB,  $^{18}\text{F}$ -Florbetapir) helps explain why  
863 cognitive decline correlates better with tau pathology and synapse loss than with brain  
864 amyloid detection. The form of  $\beta$ -amyloid in the brain is more critical than the amount,  
865 and Trem2-mediated microgliosis facilitates the consolidation of  $\beta$ -amyloid into a highly  
866 compacted, less damaging form. Therefore, therapeutics that enhance this microglial  
867 activity may prevent AD or delay its progression while simultaneously (and perhaps  
868 counterintuitively) leading to increases in PET signals for amyloid content and  
869 microgliosis. Clinical biomarkers of neuronal degeneration and spreading AD pathology  
870 such as neurofilament-L and tau should be more informative indicators of whether a  
871 microglia-directed therapy is achieving efficacy.

872 **Author contributions**

873 WJM, AE, MS and DVH conceived the overall studies. WJM, JI, TW, MW, KLS, AE, and  
874 DVH managed the production of experimental animal cohorts, the collection of tissues,  
875 or the outsourcing of brain tissues for mounting, sectioning and histology. KS performed  
876 brain dissociations and immunolabeling, flow cytometry or FACS, and microglial RNA  
877 purification. BAF and DVH performed bioinformatic analyses of RNAseq data. S-HL  
878 performed the X-34 stains and confocal imaging and calculated plaque diffuseness  
879 indices. PC and MK coordinated and analyzed the ELISA measurements of A $\beta$ 40 and  
880 A $\beta$ 42 peptide abundance. GL performed the staining, imaging, and quantification of dot  
881 blots for soluble A $\beta$  measurements. WJM, GL, KLS collected plasma and CSF for NfL  
882 measurements. GL and WJM performed the costaining and confocal imaging of plaque,  
883 microglia, and dystrophic axons or ApoE. HN and OF performed or managed all  
884 imaging and analysis of entire sections, and analysis of plaque diffuseness in confocal  
885 images with X-34 stains. AG, AJK and JE designed, conducted, or analyzed the two-  
886 photon imaging for dendritic spine analysis and volumetric plaque measurements. WJM  
887 performed all statistical analyses for stained sections and ELISAs. WJM and DVH wrote  
888 the manuscript with input from co-authors.

889

890

## 891 REFERENCES

892

- 893 Andorfer, C., Y. Kress, M. Espinoza, R. de Silva, K.L. Tucker, Y.A. Barde, K. Duff, and P. Davies.  
894 2003. Hyperphosphorylation and aggregation of tau in mice expressing normal  
895 human tau isoforms. *J Neurochem.* 86:582-590.
- 896 Bacioglu, M., L.F. Maia, O. Preische, J. Schelle, A. Apel, S.A. Kaeser, M. Schweighauser, T.  
897 Eninger, M. Lambert, A. Pilotto, D.R. Shimshek, U. Neumann, P.J. Kahle, M. Staufenbiel,  
898 M. Neumann, W. Maetzler, J. Kuhle, and M. Jucker. 2016. Neurofilament Light Chain  
899 in Blood and CSF as Marker of Disease Progression in Mouse Models and in  
900 Neurodegenerative Diseases. *Neuron.* 91:56-66.
- 901 Bemiller, S.M., T.J. McCray, K. Allan, S.V. Formica, G. Xu, G. Wilson, O.N. Kokiko-Cochran, S.D.  
902 Crish, C.A. Lasagna-Reeves, R.M. Ransohoff, G.E. Landreth, and B.T. Lamb. 2017.  
903 TREM2 deficiency exacerbates tau pathology through dysregulated kinase signaling  
904 in a mouse model of tauopathy. *Mol Neurodegener.* 12:74.
- 905 Berger, H., A. Wodarz, and A. Borchers. 2017. PTK7 Faces the Wnt in Development and  
906 Disease. *Front Cell Dev Biol.* 5:31.
- 907 Boerboom, D., L.D. White, S. Dalle, J. Courty, and J.S. Richards. 2006. Dominant-stable beta-  
908 catenin expression causes cell fate alterations and Wnt signaling antagonist  
909 expression in a murine granulosa cell tumor model. *Cancer Res.* 66:1964-1973.
- 910 Bouchon, A., C. Hernandez-Munain, M. Cella, and M. Colonna. 2001. A DAP12-mediated  
911 pathway regulates expression of CC chemokine receptor 7 and maturation of human  
912 dendritic cells. *J Exp Med.* 194:1111-1122.
- 913 Buchman, J.J., O. Durak, and L.H. Tsai. 2011. ASPM regulates Wnt signaling pathway activity  
914 in the developing brain. *Genes Dev.* 25:1909-1914.
- 915 Busby, V., S. Goossens, P. Nowotny, G. Hamilton, S. Smemo, D. Harold, D. Turic, L. Jehu, A.  
916 Myers, M. Womick, D. Woo, D. Compton, L.M. Doil, K.M. Tacey, K.F. Lau, S. Al-Saraj, R.  
917 Killick, S. Pickering-Brown, P. Moore, P. Hollingworth, N. Archer, C. Foy, S. Walter, C.  
918 Lendon, T. Iwatsubo, J.C. Morris, J. Norton, D. Mann, B. Janssens, J. Hardy, M.  
919 O'Donovan, L. Jones, J. Williams, P. Holmans, M.J. Owen, A. Grupe, J. Powell, J. van  
920 Hengel, A. Goate, F. Van Roy, and S. Lovestone. 2004. Alpha-T-catenin is expressed in  
921 human brain and interacts with the Wnt signaling pathway but is not responsible  
922 for linkage to chromosome 10 in Alzheimer's disease. *Neuromolecular Med.* 5:133-  
923 146.
- 924 Campbell, S.K., R.C. Switzer, and T.L. Martin. 1987. Alzheimer's plaques and tangles: a  
925 controlled and enhanced silver staining method. Soc. Neuroscience abstract, 13:678  
926 (see also U.S. Patent 5192688).
- 927 Cella, M., C. Buonsanti, C. Strader, T. Kondo, A. Salmaggi, and M. Colonna. 2003. Impaired  
928 differentiation of osteoclasts in TREM-2-deficient individuals. *J Exp Med.* 198:645-  
929 651.
- 930 Condello, C., P. Yuan, A. Schain, and J. Grutzendler. 2015. Microglia constitute a barrier that  
931 prevents neurotoxic protofibrillar Abeta42 hotspots around plaques. *Nat Commun.*  
932 6:6176.
- 933 D'Amore, J.D., S.T. Kajdasz, M.E. McLellan, B.J. Bacskai, E.A. Stern, and B.T. Hyman. 2003. In  
934 vivo multiphoton imaging of a transgenic mouse model of Alzheimer disease reveals  
935 marked thioflavine-S-associated alterations in neurite trajectories. *J Neuropathol*  
936 *Exp Neurol.* 62:137-145.

- 937 de Olmos, J.S., C.A. Beltramino, and S. de Olmos de Lorenzo. 1994. Use of an amino-cupric-  
 938 silver technique for the detection of early and semiacute neuronal degeneration  
 939 caused by neurotoxicants, hypoxia, and physical trauma. *Neurotoxicol Teratol.*  
 940 16:545-561.
- 941 Deczkowska, A., H. Keren-Shaul, A. Weiner, M. Colonna, M. Schwartz, and I. Amit. 2018.  
 942 Disease-Associated Microglia: A Universal Immune Sensor of Neurodegeneration.  
 943 *Cell.* 173:1073-1081.
- 944 Devotta, A., C.S. Hong, and J.P. Saint-Jeannet. 2018. Dkk2 promotes neural crest  
 945 specification by activating Wnt/beta-catenin signaling in a GSK3beta independent  
 946 manner. *Elife.* 7.
- 947 Diep, D.B., N. Hoen, M. Backman, O. Machon, and S. Krauss. 2004. Characterisation of the  
 948 Wnt antagonists and their response to conditionally activated Wnt signalling in the  
 949 developing mouse forebrain. *Brain Res Dev Brain Res.* 153:261-270.
- 950 Diks, S.H., R.J. Bink, S. van de Water, J. Joore, C. van Rooijen, F.J. Verbeek, J. den Hertog, M.P.  
 951 Peppelenbosch, and D. Zivkovic. 2006. The novel gene *asb11*: a regulator of the size  
 952 of the neural progenitor compartment. *J Cell Biol.* 174:581-592.
- 953 Dunn, K.W., M.M. Kamocka, and J.H. McDonald. 2011. A practical guide to evaluating  
 954 colocalization in biological microscopy. *Am J Physiol Cell Physiol.* 300:C723-742.
- 955 Focke, C., T. Blume, B. Zott, Y. Shi, M. Deussing, F. Peters, C. Schmidt, G. Kleinberger, S.  
 956 Lindner, F.J. Gildehaus, L. Beyer, B. von Ungern-Sternberg, P. Bartenstein, L. Ozmen,  
 957 K. Baumann, M.M. Dorostkar, C. Haass, H. Adelsberger, J. Herms, A. Rominger, and M.  
 958 Brendel. 2019. Early and Longitudinal Microglial Activation but Not Amyloid  
 959 Accumulation Predicts Cognitive Outcome in PS2APP Mice. *J Nucl Med.* 60:548-554.
- 960 Fonseca, M.I., J. Zhou, M. Botto, and A.J. Tenner. 2004. Absence of C1q leads to less  
 961 neuropathology in transgenic mouse models of Alzheimer's disease. *J Neurosci.*  
 962 24:6457-6465.
- 963 Friedman, B.A., K. Srinivasan, G. Ayalon, W.J. Meilandt, H. Lin, M.A. Huntley, Y. Cao, S.H. Lee,  
 964 P.C.G. Haddick, H. Ngu, Z. Modrusan, J.L. Larson, J.S. Kaminker, M.P. van der Brug,  
 965 and D.V. Hansen. 2018. Diverse Brain Myeloid Expression Profiles Reveal Distinct  
 966 Microglial Activation States and Aspects of Alzheimer's Disease Not Evident in  
 967 Mouse Models. *Cell Rep.* 22:832-847.
- 968 Gage, P.J., M. Qian, D. Wu, and K.I. Rosenberg. 2008. The canonical Wnt signaling antagonist  
 969 DKK2 is an essential effector of PITX2 function during normal eye development. *Dev*  
 970 *Biol.* 317:310-324.
- 971 Gowrishankar, S., P. Yuan, Y. Wu, M. Schrag, S. Paradise, J. Grutzendler, P. De Camilli, and  
 972 S.M. Ferguson. 2015. Massive accumulation of luminal protease-deficient axonal  
 973 lysosomes at Alzheimer's disease amyloid plaques. *Proc Natl Acad Sci U S A.*  
 974 112:E3699-3708.
- 975 Gratuze, M., C.E.G. Leyns, and D.M. Holtzman. 2018. New insights into the role of TREM2 in  
 976 Alzheimer's disease. *Mol Neurodegener.* 13:66.
- 977 Grieciuc, A., S. Patel, A.N. Federico, S.H. Choi, B.J. Innes, M.K. Oram, G. Cereghetti, D. McGinty,  
 978 A. Anselmo, R.I. Sadreyev, S.E. Hickman, J. El Khoury, M. Colonna, and R.E. Tanzi.  
 979 2019. TREM2 Acts Downstream of CD33 in Modulating Microglial Pathology in  
 980 Alzheimer's Disease. *Neuron.* 103:820-835 e827.
- 981 Guerreiro, R., A. Wojtas, J. Bras, M. Carrasquillo, E. Rogaeva, E. Majounie, C. Cruchaga, C.  
 982 Sassi, J.S. Kauwe, S. Younkin, L. Hazrati, J. Collinge, J. Pocock, T. Lashley, J. Williams,

- 983 J.C. Lambert, P. Amouyel, A. Goate, R. Rademakers, K. Morgan, J. Powell, P. St George-  
984 Hyslop, A. Singleton, J. Hardy, and G. Alzheimer Genetic Analysis. 2013. TREM2  
985 variants in Alzheimer's disease. *N Engl J Med*. 368:117-127.
- 986 Haass, C., and D.J. Selkoe. 2007. Soluble protein oligomers in neurodegeneration: lessons  
987 from the Alzheimer's amyloid beta-peptide. *Nat Rev Mol Cell Biol*. 8:101-112.
- 988 Hamelin, L., J. Lagarde, G. Dorothee, C. Leroy, M. Labit, R.A. Comley, L.C. de Souza, H. Corne,  
989 L. Dauphinot, M. Bertoux, B. Dubois, P. Gervais, O. Colliot, M.C. Potier, M. Bottlaender,  
990 M. Sarazin, and I.t. Clinical. 2016. Early and protective microglial activation in  
991 Alzheimer's disease: a prospective study using 18F-DPA-714 PET imaging. *Brain*.  
992 139:1252-1264.
- 993 Hansen, D.V., J.E. Hanson, and M. Sheng. 2018. Microglia in Alzheimer's disease. *J Cell Biol*.  
994 217:459-472.
- 995 He, Z., J.L. Guo, J.D. McBride, S. Narasimhan, H. Kim, L. Changolkar, B. Zhang, R.J. Gathagan, C.  
996 Yue, C. Dengler, A. Stieber, M. Nitla, D.A. Coulter, T. Abel, K.R. Brunden, J.Q.  
997 Trojanowski, and V.M. Lee. 2018. Amyloid-beta plaques enhance Alzheimer's brain  
998 tau-seeded pathologies by facilitating neuritic plaque tau aggregation. *Nat Med*.  
999 24:29-38.
- 1000 Heneka, M.T., M.J. Carson, J. El Khoury, G.E. Landreth, F. Brosseron, D.L. Feinstein, A.H.  
1001 Jacobs, T. Wyss-Coray, J. Vitorica, R.M. Ransohoff, K. Herrup, S.A. Frautschy, B. Finsen,  
1002 G.C. Brown, A. Verkhratsky, K. Yamanaka, J. Koistinaho, E. Latz, A. Halle, G.C. Petzold,  
1003 T. Town, D. Morgan, M.L. Shinohara, V.H. Perry, C. Holmes, N.G. Bazan, D.J. Brooks, S.  
1004 Hunot, B. Joseph, N. Deigendesch, O. Garaschuk, E. Boddeke, C.A. Dinarello, J.C.  
1005 Breitner, G.M. Cole, D.T. Golenbock, and M.P. Kummer. 2015. Neuroinflammation in  
1006 Alzheimer's disease. *Lancet Neurol*. 14:388-405.
- 1007 Hong, S., V.F. Beja-Glasser, B.M. Nfonoyim, A. Frouin, S. Li, S. Ramakrishnan, K.M. Merry, Q.  
1008 Shi, A. Rosenthal, B.A. Barres, C.A. Lemere, D.J. Selkoe, and B. Stevens. 2016.  
1009 Complement and microglia mediate early synapse loss in Alzheimer mouse models.  
1010 *Science*. 352:712-716.
- 1011 Hsieh, J.C., L. Kodjabachian, M.L. Rebbert, A. Rattner, P.M. Smallwood, C.H. Samos, R. Nusse,  
1012 I.B. Dawid, and J. Nathans. 1999. A new secreted protein that binds to Wnt proteins  
1013 and inhibits their activities. *Nature*. 398:431-436.
- 1014 Itzhaki, R.F., R. Lathe, B.J. Balin, M.J. Ball, E.L. Bearer, H. Braak, M.J. Bullido, C. Carter, M.  
1015 Clerici, S.L. Cosby, K. Del Tredici, H. Field, T. Fulop, C. Grassi, W.S. Griffin, J. Haas, A.P.  
1016 Hudson, A.R. Kamer, D.B. Kell, F. Licastro, L. Letenneur, H. Lovheim, R. Mancuso, J.  
1017 Miklossy, C. Otth, A.T. Palamara, G. Perry, C. Preston, E. Pretorius, T. Strandberg, N.  
1018 Tabet, S.D. Taylor-Robinson, and J.A. Whittum-Hudson. 2016. Microbes and  
1019 Alzheimer's Disease. *J Alzheimers Dis*. 51:979-984.
- 1020 Jack, C.R., Jr., H.J. Wiste, C.G. Schwarz, V.J. Lowe, M.L. Senjem, P. Vemuri, S.D. Weigand, T.M.  
1021 Therneau, D.S. Knopman, J.L. Gunter, D.T. Jones, J. Graff-Radford, K. Kantarci, R.O.  
1022 Roberts, M.M. Mielke, M.M. Machulda, and R.C. Petersen. 2018. Longitudinal tau PET  
1023 in ageing and Alzheimer's disease. *Brain*. 141:1517-1528.
- 1024 Jacobs, H.I.L., T. Hedden, A.P. Schultz, J. Sepulcre, R.D. Perea, R.E. Amariglio, K.V. Papp, D.M.  
1025 Rentz, R.A. Sperling, and K.A. Johnson. 2018. Structural tract alterations predict  
1026 downstream tau accumulation in amyloid-positive older individuals. *Nat Neurosci*.  
1027 21:424-431.

- 1028 Jay, T.R., A.M. Hirsch, M.L. Broihier, C.M. Miller, L.E. Neilson, R.M. Ransohoff, B.T. Lamb, and  
 1029 G.E. Landreth. 2017a. Disease Progression-Dependent Effects of TREM2 Deficiency  
 1030 in a Mouse Model of Alzheimer's Disease. *J Neurosci*. 37:637-647.
- 1031 Jay, T.R., C.M. Miller, P.J. Cheng, L.C. Graham, S. Bemiller, M.L. Broihier, G. Xu, D. Margevicius,  
 1032 J.C. Karlo, G.L. Sousa, A.C. Coteleur, O. Butovsky, L. Bekris, S.M. Staugaitis, J.B.  
 1033 Leverenz, S.W. Pimplikar, G.E. Landreth, G.R. Howell, R.M. Ransohoff, and B.T. Lamb.  
 1034 2015. TREM2 deficiency eliminates TREM2+ inflammatory macrophages and  
 1035 ameliorates pathology in Alzheimer's disease mouse models. *J Exp Med*. 212:287-  
 1036 295.
- 1037 Jay, T.R., V.E. von Saucken, and G.E. Landreth. 2017b. TREM2 in Neurodegenerative  
 1038 Diseases. *Mol Neurodegener*. 12:56.
- 1039 Jonsson, T., H. Stefansson, S. Steinberg, I. Jonsdottir, P.V. Jonsson, J. Snaedal, S. Bjornsson, J.  
 1040 Huttenlocher, A.I. Levey, J.J. Lah, D. Rujescu, H. Hampel, I. Giegling, O.A. Andreassen,  
 1041 K. Engedal, I. Ulstein, S. Djurovic, C. Ibrahim-Verbaas, A. Hofman, M.A. Ikram, C.M.  
 1042 van Duijn, U. Thorsteinsdottir, A. Kong, and K. Stefansson. 2013. Variant of TREM2  
 1043 associated with the risk of Alzheimer's disease. *N Engl J Med*. 368:107-116.
- 1044 Kallop, D.Y., W.J. Meilandt, A. Gogineni, C. Easley-Neal, T. Wu, A.M. Jubbs, M. Yaylaoglu, M.  
 1045 Shamloo, M. Tessier-Lavigne, K. Searce-Levie, and R.M. Weimer. 2014. A death  
 1046 receptor 6-amyloid precursor protein pathway regulates synapse density in the  
 1047 mature CNS but does not contribute to Alzheimer's disease-related pathophysiology  
 1048 in murine models. *J Neurosci*. 34:6425-6437.
- 1049 Kang, S.S., A. Kurti, K.E. Baker, C.C. Liu, M. Colonna, J.D. Ulrich, D.M. Holtzman, G. Bu, and J.D.  
 1050 Fryer. 2018. Behavioral and transcriptomic analysis of Trem2-null mice: not all  
 1051 knockout mice are created equal. *Hum Mol Genet*. 27:211-223.
- 1052 Karasawa, T., H. Yokokura, J. Kitajewski, and P.J. Lombroso. 2002. Frizzled-9 is activated by  
 1053 Wnt-2 and functions in Wnt/beta-catenin signaling. *J Biol Chem*. 277:37479-37486.
- 1054 Keren-Shaul, H., A. Spinrad, A. Weiner, O. Matcovitch-Natan, R. Dvir-Szternfeld, T.K. Ulland,  
 1055 E. David, K. Baruch, D. Lara-Astaiso, B. Toth, S. Itzkovitz, M. Colonna, M. Schwartz,  
 1056 and I. Amit. 2017. A Unique Microglia Type Associated with Restricting  
 1057 Development of Alzheimer's Disease. *Cell*. 169:1276-1290 e1217.
- 1058 Khalil, M., C.E. Teunissen, M. Otto, F. Piehl, M.P. Sormani, T. Gatringer, C. Barro, L. Kappos,  
 1059 M. Comabella, F. Fazekas, A. Petzold, K. Blennow, H. Zetterberg, and J. Kuhle. 2018.  
 1060 Neurofilaments as biomarkers in neurological disorders. *Nat Rev Neurol*. 14:577-  
 1061 589.
- 1062 Kim, J., A.E. Eltorai, H. Jiang, F. Liao, P.B. Verghese, J. Kim, F.R. Stewart, J.M. Basak, and D.M.  
 1063 Holtzman. 2012. Anti-apoE immunotherapy inhibits amyloid accumulation in a  
 1064 transgenic mouse model of Abeta amyloidosis. *J Exp Med*. 209:2149-2156.
- 1065 Klein, W.L. 2002. Abeta toxicity in Alzheimer's disease: globular oligomers (ADDLs) as new  
 1066 vaccine and drug targets. *Neurochem Int*. 41:345-352.
- 1067 Klunk, W.E., B.J. Bacskaï, C.A. Mathis, S.T. Kajdasz, M.E. McLellan, M.P. Frosch, M.L. Debnath,  
 1068 D.P. Holt, Y. Wang, and B.T. Hyman. 2002. Imaging Abeta plaques in living transgenic  
 1069 mice with multiphoton microscopy and methoxy-X04, a systemically administered  
 1070 Congo red derivative. *J Neuropathol Exp Neurol*. 61:797-805.
- 1071 Krasemann, S., C. Madore, R. Cialic, C. Baufeld, N. Calcagno, R. El Fatimy, L. Beckers, E.  
 1072 O'Loughlin, Y. Xu, Z. Fanek, D.J. Greco, S.T. Smith, G. Tweet, Z. Humulock, T. Zrzavy, P.  
 1073 Conde-Sanroman, M. Gacias, Z. Weng, H. Chen, E. Tjon, F. Mazaheri, K. Hartmann, A.

- 1074 Madi, J.D. Ulrich, M. Glatzel, A. Worthmann, J. Heeren, B. Budnik, C. Lemere, T. Ikezu,  
1075 F.L. Heppner, V. Litvak, D.M. Holtzman, H. Lassmann, H.L. Weiner, J. Ochando, C.  
1076 Haass, and O. Butovsky. 2017. The TREM2-APOE Pathway Drives the  
1077 Transcriptional Phenotype of Dysfunctional Microglia in Neurodegenerative  
1078 Diseases. *Immunity*. 47:566-581 e569.
- 1079 Krstic, D., and I. Knuesel. 2013. The airbag problem-a potential culprit for bench-to-bedside  
1080 translational efforts: relevance for Alzheimer's disease. *Acta Neuropathol Commun*.  
1081 1:62.
- 1082 Lai, J.P., A.M. Oseini, C.D. Moser, C. Yu, S.F. Elsawa, C. Hu, I. Nakamura, T. Han, I. Aderca, H.  
1083 Isomoto, M.M. Garrity-Park, A.M. Shire, J. Li, S.O. Sanderson, A.A. Adjei, M.E.  
1084 Fernandez-Zapico, and L.R. Roberts. 2010. The oncogenic effect of sulfatase 2 in  
1085 human hepatocellular carcinoma is mediated in part by glypican 3-dependent Wnt  
1086 activation. *Hepatology*. 52:1680-1689.
- 1087 Law, C.W., Y.S. Chen, W. Shi, and G.K. Smyth. 2014. voom: precision weights unlock linear  
1088 model analysis tools for RNA-seq read counts. *Genome Biol*. 15.
- 1089 Le Pichon, C.E., S.L. Dominguez, H. Solanoy, H. Ngu, N. Lewin-Koh, M. Chen, J. Eastham-  
1090 Anderson, R. Watts, and K. Scearce-Levie. 2013. EGFR inhibitor erlotinib delays  
1091 disease progression but does not extend survival in the SOD1 mouse model of ALS.  
1092 *PLoS One*. 8:e62342.
- 1093 Lessard, C.B., S.L. Malnik, Y. Zhou, T.B. Ladd, P.E. Cruz, Y. Ran, T.E. Mahan, P. Chakrabaty,  
1094 D.M. Holtzman, J.D. Ulrich, M. Colonna, and T.E. Golde. 2018. High-affinity  
1095 interactions and signal transduction between Abeta oligomers and TREM2. *EMBO  
1096 Mol Med*. 10.
- 1097 Leyns, C.E.G., M. Gratuze, S. Narasimhan, N. Jain, L.J. Koscal, H. Jiang, M. Manis, M. Colonna,  
1098 V.M.Y. Lee, J.D. Ulrich, and D.M. Holtzman. 2019. TREM2 function impedes tau  
1099 seeding in neuritic plaques. *Nat Neurosci*.
- 1100 Leyns, C.E.G., J.D. Ulrich, M.B. Finn, F.R. Stewart, L.J. Koscal, J. Remolina Serrano, G.O.  
1101 Robinson, E. Anderson, M. Colonna, and D.M. Holtzman. 2017. TREM2 deficiency  
1102 attenuates neuroinflammation and protects against neurodegeneration in a mouse  
1103 model of tauopathy. *Proc Natl Acad Sci U S A*. 114:11524-11529.
- 1104 Lin, Z., C. Gao, Y. Ning, X. He, W. Wu, and Y.G. Chen. 2008. The pseudoreceptor BMP and  
1105 activin membrane-bound inhibitor positively modulates Wnt/beta-catenin signaling.  
1106 *J Biol Chem*. 283:33053-33058.
- 1107 Love, M.I., W. Huber, and S. Anders. 2014. Moderated estimation of fold change and  
1108 dispersion for RNA-seq data with DESeq2. *Genome Biol*. 15.
- 1109 Mao, B., and C. Niehrs. 2003. Kremen2 modulates Dickkopf2 activity during Wnt/LRP6  
1110 signaling. *Gene*. 302:179-183.
- 1111 Mazaheri, F., N. Snaidero, G. Kleinberger, C. Madore, A. Daria, G. Werner, S. Krasemann, A.  
1112 Capell, D. Trumbach, W. Wurst, B. Brunner, S. Bultmann, S. Tahirovic, M.  
1113 Kerschensteiner, T. Misgeld, O. Butovsky, and C. Haass. 2017. TREM2 deficiency  
1114 impairs chemotaxis and microglial responses to neuronal injury. *EMBO Rep*.  
1115 18:1186-1198.
- 1116 Meilandt, W.J., J.A. Maloney, J. Imperio, G. Lalehzadeh, T. Earr, S. Crowell, T.W. Bainbridge, Y.  
1117 Lu, J.A. Ernst, R.N. Fuji, and J. Atwal. 2019. Characterization of the selective in vitro  
1118 and in vivo binding properties of crenezumab to oligomeric A $\beta$ . *Alzheimers Res Ther*.  
1119 In press.

- 1120 Mi, H., A. Muruganujan, D. Ebert, X. Huang, and P.D. Thomas. 2019. PANTHER version 14:  
1121 more genomes, a new PANTHER GO-slim and improvements in enrichment analysis  
1122 tools. *Nucleic Acids Res.* 47:D419-D426.
- 1123 Morris, G.P., I.A. Clark, and B. Vissel. 2014. Inconsistencies and controversies surrounding  
1124 the amyloid hypothesis of Alzheimer's disease. *Acta Neuropathol Commun.* 2:135.
- 1125 Olmos-Alonso, A., S.T. Schettters, S. Sri, K. Askew, R. Mancuso, M. Vargas-Caballero, C.  
1126 Holscher, V.H. Perry, and D. Gomez-Nicola. 2016. Pharmacological targeting of  
1127 CSF1R inhibits microglial proliferation and prevents the progression of Alzheimer's-  
1128 like pathology. *Brain.* 139:891-907.
- 1129 Orre, M., W. Kamphuis, L.M. Osborn, A.H.P. Jansen, L. Kooijman, K. Bossers, and E.M. Hol.  
1130 2014. Isolation of glia from Alzheimer's mice reveals inflammation and dysfunction.  
1131 *Neurobiol Aging.* 35:2746-2760.
- 1132 Ozmen, L., A. Albientz, C. Czech, and H. Jacobsen. 2009. Expression of transgenic APP mRNA  
1133 is the key determinant for beta-amyloid deposition in PS2APP transgenic mice.  
1134 *Neurodegener Dis.* 6:29-36.
- 1135 Paloneva, J., J. Mandelin, A. Kiialainen, T. Bohling, J. Prudlo, P. Hakola, M. Haltia, Y.T.  
1136 Konttinen, and L. Peltonen. 2003. DAP12/TREM2 deficiency results in impaired  
1137 osteoclast differentiation and osteoporotic features. *J Exp Med.* 198:669-675.
- 1138 Parhizkar, S., T. Arzberger, M. Brendel, G. Kleinberger, M. Deussing, C. Focke, B. Nuscher, M.  
1139 Xiong, A. Ghasemigharagoz, N. Katzmarski, S. Krasemann, S.F. Lichtenthaler, S.A.  
1140 Muller, A. Colombo, L.S. Monasor, S. Tahirovic, J. Herms, M. Willem, N. Pettkus, O.  
1141 Butovsky, P. Bartenstein, D. Edbauer, A. Rominger, A. Erturk, S.A. Grathwohl, J.J.  
1142 Neher, D.M. Holtzman, M. Meyer-Luehmann, and C. Haass. 2019. Loss of TREM2  
1143 function increases amyloid seeding but reduces plaque-associated ApoE. *Nat*  
1144 *Neurosci.* 22:191-204.
- 1145 Park, J., I. Wetzel, I. Marriott, D. Dreau, C. D'Avanzo, D.Y. Kim, R.E. Tanzi, and H. Cho. 2018. A  
1146 3D human triculture system modeling neurodegeneration and neuroinflammation  
1147 in Alzheimer's disease. *Nat Neurosci.* 21:941-951.
- 1148 Poliani, P.L., Y. Wang, E. Fontana, M.L. Robinette, Y. Yamanishi, S. Gilfillan, and M. Colonna.  
1149 2015. TREM2 sustains microglial expansion during aging and response to  
1150 demyelination. *J Clin Invest.* 125:2161-2170.
- 1151 Pooler, A.M., M. Polydoro, E.A. Maury, S.B. Nicholls, S.M. Reddy, S. Wegmann, C. William, L.  
1152 Saqran, O. Cagsal-Getkin, R. Pitstick, D.R. Beier, G.A. Carlson, T.L. Spires-Jones, and  
1153 B.T. Hyman. 2015. Amyloid accelerates tau propagation and toxicity in a model of  
1154 early Alzheimer's disease. *Acta Neuropathol Commun.* 3:14.
- 1155 Shi, Q., S. Chowdhury, R. Ma, K.X. Le, S. Hong, B.J. Caldarone, B. Stevens, and C.A. Lemere.  
1156 2017. Complement C3 deficiency protects against neurodegeneration in aged  
1157 plaque-rich APP/PS1 mice. *Sci Transl Med.* 9.
- 1158 Spangenberg, E.E., R.J. Lee, A.R. Najafi, R.A. Rice, M.R. Elmore, M. Blurton-Jones, B.L. West,  
1159 and K.N. Green. 2016. Eliminating microglia in Alzheimer's mice prevents neuronal  
1160 loss without modulating amyloid-beta pathology. *Brain.* 139:1265-1281.
- 1161 Spires, T.L., and B.T. Hyman. 2004. Neuronal structure is altered by amyloid plaques. *Rev*  
1162 *Neurosci.* 15:267-278.
- 1163 Spires, T.L., M. Meyer-Luehmann, E.A. Stern, P.J. McLean, J. Skoch, P.T. Nguyen, B.J. Bacskai,  
1164 and B.T. Hyman. 2005. Dendritic spine abnormalities in amyloid precursor protein

- 1165 transgenic mice demonstrated by gene transfer and intravital multiphoton  
 1166 microscopy. *J Neurosci.* 25:7278-7287.
- 1167 Srinivasan, K., B.A. Friedman, J.L. Larson, B.E. Lauffer, L.D. Goldstein, L.L. Appling, J. Borneo,  
 1168 C. Poon, T. Ho, F. Cai, P. Steiner, M.P. van der Brug, Z. Modrusan, J.S. Kaminker, and  
 1169 D.V. Hansen. 2016. Untangling the brain's neuroinflammatory and  
 1170 neurodegenerative transcriptional responses. *Nat Commun.* 7:11295.
- 1171 Switzer, R.C., 3rd. 2000. Application of silver degeneration stains for neurotoxicity testing.  
 1172 *Toxicol Pathol.* 28:70-83.
- 1173 Switzer, R.C., S.K. Campbell, and T.M. Murdock. 1993. A histologic method for staining  
 1174 Alzheimer pathology. U.S. Patent 5192688.
- 1175 Tee, J.M., M.A. Sartori da Silva, A.M. Rygiel, V. Muncan, R. Bink, G.R. van den Brink, P. van  
 1176 Tijn, D. Zivkovic, L.L. Kodach, D. Guardavaccaro, S.H. Diks, and M.P. Peppelenbosch.  
 1177 2012. asb11 is a regulator of embryonic and adult regenerative myogenesis. *Stem*  
 1178 *Cells Dev.* 21:3091-3103.
- 1179 Tomic, J.L., A. Pensalfini, E. Head, and C.G. Glabe. 2009. Soluble fibrillar oligomer levels are  
 1180 elevated in Alzheimer's disease brain and correlate with cognitive dysfunction.  
 1181 *Neurobiol Dis.* 35:352-358.
- 1182 Tsai, J., J. Grutzendler, K. Duff, and W.B. Gan. 2004. Fibrillar amyloid deposition leads to  
 1183 local synaptic abnormalities and breakage of neuronal branches. *Nat Neurosci.*  
 1184 7:1181-1183.
- 1185 Turnbull, I.R., S. Gilfillan, M. Cella, T. Aoshi, M. Miller, L. Piccio, M. Hernandez, and M.  
 1186 Colonna. 2006. Cutting edge: TREM-2 attenuates macrophage activation. *J Immunol.*  
 1187 177:3520-3524.
- 1188 Ulland, T.K., and M. Colonna. 2018. TREM2 - a key player in microglial biology and  
 1189 Alzheimer disease. *Nat Rev Neurol.* 14:667-675.
- 1190 Ulland, T.K., W.M. Song, S.C. Huang, J.D. Ulrich, A. Sergushichev, W.L. Beatty, A.A. Loboda, Y.  
 1191 Zhou, N.J. Cairns, A. Kambal, E. Loginicheva, S. Gilfillan, M. Cella, H.W. Virgin, E.R.  
 1192 Unanue, Y. Wang, M.N. Artyomov, D.M. Holtzman, and M. Colonna. 2017. TREM2  
 1193 Maintains Microglial Metabolic Fitness in Alzheimer's Disease. *Cell.* 170:649-663  
 1194 e613.
- 1195 Ulrich, J.D., T.K. Ulland, M. Colonna, and D.M. Holtzman. 2017. Elucidating the Role of  
 1196 TREM2 in Alzheimer's Disease. *Neuron.* 94:237-248.
- 1197 Wang, A., P. Das, R.C. Switzer, 3rd, T.E. Golde, and J.L. Jankowsky. 2011. Robust amyloid  
 1198 clearance in a mouse model of Alzheimer's disease provides novel insights into the  
 1199 mechanism of amyloid-beta immunotherapy. *J Neurosci.* 31:4124-4136.
- 1200 Wang, Y., M. Cella, K. Mallinson, J.D. Ulrich, K.L. Young, M.L. Robinette, S. Gilfillan, G.M.  
 1201 Krishnan, S. Sudhakar, B.H. Zinselmeyer, D.M. Holtzman, J.R. Cirrito, and M. Colonna.  
 1202 2015. TREM2 lipid sensing sustains the microglial response in an Alzheimer's  
 1203 disease model. *Cell.* 160:1061-1071.
- 1204 Wang, Y., T.K. Ulland, J.D. Ulrich, W. Song, J.A. Tzaferis, J.T. Hole, P. Yuan, T.E. Mahan, Y. Shi, S.  
 1205 Gilfillan, M. Cella, J. Grutzendler, R.B. DeMattos, J.R. Cirrito, D.M. Holtzman, and M.  
 1206 Colonna. 2016. TREM2-mediated early microglial response limits diffusion and  
 1207 toxicity of amyloid plaques. *J Exp Med.* 213:667-675.
- 1208 Wu, T., B. Dejanovic, V.D. Gandham, A. Gogineni, R. Edmonds, S. Schauer, K. Srinivasan, M.A.  
 1209 Huntley, Y. Wang, T.M. Wang, M. Hedehus, K.H. Barck, M. Stark, H. Ngu, O. Foreman,  
 1210 W.J. Meilandt, J. Elstrott, M.C. Chang, D.V. Hansen, R.A.D. Carano, M. Sheng, and J.E.

- 1211 Hanson. 2019. Complement C3 Is Activated in Human AD Brain and Is Required for  
1212 Neurodegeneration in Mouse Models of Amyloidosis and Tauopathy. *Cell Rep.*  
1213 28:2111-2123 e2116.
- 1214 Wu, T.D., J. Reeder, M. Lawrence, G. Becker, and M.J. Brauer. 2016. GMAP and GSNAP for  
1215 Genomic Sequence Alignment: Enhancements to Speed, Accuracy, and Functionality.  
1216 *Methods Mol Biol.* 1418:283-334.
- 1217 Wu, W., A. Glinka, H. Delius, and C. Niehrs. 2000. Mutual antagonism between dickkopf1  
1218 and dickkopf2 regulates Wnt/beta-catenin signalling. *Curr Biol.* 10:1611-1614.
- 1219 Yeh, F.L., D.V. Hansen, and M. Sheng. 2017. TREM2, Microglia, and Neurodegenerative  
1220 Diseases. *Trends Mol Med.* 23:512-533.
- 1221 Yeh, F.L., Y. Wang, I. Tom, L.C. Gonzalez, and M. Sheng. 2016. TREM2 Binds to  
1222 Apolipoproteins, Including APOE and CLU/APOJ, and Thereby Facilitates Uptake of  
1223 Amyloid-Beta by Microglia. *Neuron.* 91:328-340.
- 1224 Yoshiyama, Y., M. Higuchi, B. Zhang, S.M. Huang, N. Iwata, T.C. Saido, J. Maeda, T. Suhara, J.Q.  
1225 Trojanowski, and V.M. Lee. 2007. Synapse loss and microglial activation precede  
1226 tangles in a P301S tauopathy mouse model. *Neuron.* 53:337-351.
- 1227 Yuan, P., C. Condello, C.D. Keene, Y. Wang, T.D. Bird, S.M. Paul, W. Luo, M. Colonna, D.  
1228 Baddeley, and J. Grutzendler. 2016. TREM2 Haplodeficiency in Mice and Humans  
1229 Impairs the Microglia Barrier Function Leading to Decreased Amyloid Compaction  
1230 and Severe Axonal Dystrophy. *Neuron.* 92:252-264.
- 1231 Zhao, Y., X. Wu, X. Li, L.L. Jiang, X. Gui, Y. Liu, Y. Sun, B. Zhu, J.C. Pina-Crespo, M. Zhang, N.  
1232 Zhang, X. Chen, G. Bu, Z. An, T.Y. Huang, and H. Xu. 2018. TREM2 Is a Receptor for  
1233 beta-Amyloid that Mediates Microglial Function. *Neuron.* 97:1023-1031 e1027.
- 1234 Zheng, H., L. Jia, C.C. Liu, Z. Rong, L. Zhong, L. Yang, X.F. Chen, J.D. Fryer, X. Wang, Y.W. Zhang,  
1235 H. Xu, and G. Bu. 2017. TREM2 Promotes Microglial Survival by Activating  
1236 Wnt/beta-Catenin Pathway. *J Neurosci.* 37:1772-1784.
- 1237 Zulfiqar, S., and G. Tanriver. 2017. beta-Catenin Pathway Is Involved in TREM2-Mediated  
1238 Microglial Survival. *J Neurosci.* 37:7073-7075.
- 1239  
1240  
1241

1242 **FIGURE LEGENDS**

1243

1244 **Figure 1.** *Trem2* deletion impairs microglial clustering, activation, and plaque uptake in  
 1245 PS2APP  $\beta$ -amyloidosis model. **A**, Immunohistochemical detection of microglial clustering in  
 1246 transgenic PS2APP mice or non-transgenic (Ntg) controls with either wild type (wt),  
 1247 heterozygous (het) or homozygous knockout (ko) *Trem2* alleles. (See Figure 1-1 for analysis of  
 1248 total, rather than clustered, Iba1 signal.) Quantification of the percent area covered by clusters  
 1249 of Iba1<sup>+</sup> microglia was measured from coronal sections of female mice at 4 months (mo), 6-7mo,  
 1250 and 12mo ages, and from male mice at 6-7mo and 19-22mo ages. Each data point represents  
 1251 the composite (average) histological score from several sections of an individual mouse. Bars  
 1252 and lines represent mean  $\pm$  SEM. Significant differences between groups were determined by  
 1253 unpaired t-test for most cohorts, or by ANOVA followed by Tukey's multiple comparison test for  
 1254 the 19-22mo cohort with three genotypes (\*p<0.05, \*\*p<0.01, \*\*\*p<0.001, \*\*\*\*p<0.0001 versus  
 1255 PS2APP;Trem2<sup>wt</sup> or as indicated). **B**, Representative low (left, scale bar = 400  $\mu$ m) and high  
 1256 (right, scale bar = 100  $\mu$ m) magnification images of Iba1<sup>+</sup> staining in 12mo female mice are  
 1257 shown. Iba1<sup>+</sup> clusters (red arrowheads) showed reduced presence across Trem2<sup>ko</sup> mice at all  
 1258 ages. **C** and **D**, Like panels **A** and **B** except analyzing active microglial lysosomes as indicated  
 1259 by CD68 protein expression. **E**, Representative flow cytometry plots measuring CD45  
 1260 immunoreactivity (low or high) of CD11b<sup>+</sup> brain-resident myeloid cells from 14mo PS2APP mice  
 1261 with or without Trem2 and from Ntg mice. **F**, Percent of brain-resident myeloid cells with high  
 1262 CD45 expression measured from several mice of each genotype, with bars and lines  
 1263 representing mean  $\pm$  SEM. **G** and **H**, Like panels **E** and **F** except analyzing plaque content in  
 1264 brain CD11b<sup>+</sup> cells from ~12mo mice injected with methoxy-X04 dye to stain amyloid material.  
 1265 Ntg mice are not plotted in **H** since they have zero methoxy labeling. n=3 in Trem2<sup>wt</sup>, n=2 in  
 1266 Trem2<sup>ko</sup>. (Also see Figure 1-1 for histological analysis of methoxy-X04 and Iba1<sup>+</sup> microglia  
 1267 colocalization in sections.)

1268

1269 **Figure 2.** Induction of Neurodegeneration-related and Proliferation gene modules and Wnt-  
 1270 related signaling components is impaired in Trem2<sup>ko</sup> microglia. **A**, Heat map of differentially  
 1271 expressed genes (DEGs) between Trem2<sup>wt</sup> and Trem2<sup>ko</sup> microglia from 14mo PS2APP mouse  
 1272 brains (fold change  $\geq$  2, adjusted p  $\leq$  0.05), cross-referenced against previously published  
 1273 datasets from the PS2APP (GSE89482), APPswe/PS1de9 (GSE74615), and 5xFAD  
 1274 (GSE65067) models. Each row is a DEG, and each column is a microglial sort from a different  
 1275 mouse. Z-score coloring represents a sample's distance in standard deviations from the mean

1276 expression value for a given gene across samples within a dataset. Most of the downregulated  
1277 DEGs in Trem2<sup>ko</sup> microglia were typically induced in models of  $\beta$ -amyloid pathology, and the  
1278 majority also showed impaired microglial induction in Trem2<sup>ko</sup> 5xFAD mice. See Figure 2-1  
1279 Extended Data table for a complete list of genome-wide expression values in PS2APP;Trem2<sup>wt</sup>  
1280 and PS2APP;Trem2<sup>ko</sup> microglia. **B**, Induction of the Wnt/proliferation regulators *Dkk2*, *Wif1*,  
1281 *Ctnna3*, and *Asb11* were completely impaired in Trem2<sup>ko</sup> microglia of PS2APP mice. **C**, DEGs  
1282 identified by GO analysis as “Positive Regulators of Wnt Signaling” with reduced expression in  
1283 PS2APP;Trem2<sup>ko</sup> microglia included *Fzd9*, *Sulf2*, *Bambi*, *Ptk7*, *Aspm*, and *Dkk2*. Bars and lines  
1284 in **B** and **C** represent mean  $\pm$  SEM, with each data point representing microglial gene  
1285 expression level from a given mouse. For genes depicted in **B** and **C**, see also Figure 2-2  
1286 showing microglial expression in the 5xFAD model with or without Trem2 (data from  
1287 independent investigators). **D**, (top) Analysis of previously published expression profiles from  
1288 the PS2APP model (GSE89482) indicated that six gene expression modules for brain myeloid  
1289 cells (defined in Friedman et al., 2018) showed altered expression in microglia from brains with  
1290  $\beta$ -amyloid pathology. (bottom) Analysis of Trem2<sup>ko</sup> and Trem2<sup>wt</sup> microglia expression profiles  
1291 from PS2APP mice showed that the Neurodegeneration-related and Proliferation gene sets  
1292 showed significant Trem2 dependence. (See also Figure 2-2 for data from independent  
1293 investigators showing enriched expression of Proliferation module in 5xFAD model microglia  
1294 and its dependence on Trem2 for full induction. See also Figure 2-3 for heat map displays of all  
1295 individual genes in each module.) Each data point represents a gene set expression score for  
1296 microglia isolated from a given mouse. Lines represent mean  $\pm$  SEM. Asterisks represent p  
1297 values (\*p<0.05, \*\*p<0.01, \*\*\*p<0.001, \*\*\*\*p<0.0001) from two-tailed t-tests assuming unequal  
1298 variance between groups. **E**, 4-way plot of Neurodegeneration-related gene set, with each point  
1299 representing a gene’s fold change in expression between PS2APP vs. non-transgenic microglia  
1300 on the x-axis (red and blue points, adjusted p < 0.05) and between PS2APP;Trem2<sup>ko</sup> vs.  
1301 PS2APP;Trem2<sup>wt</sup> microglia on the y-axis (green and blue points, adjusted p < 0.05). Blue points  
1302 showed significant differential expression in both datasets. Tiny black points represent genes  
1303 not differentially expressed in either dataset.

1304

1305 **Figure 3.** *Trem2* deletion shows age- and sex-dependent effects on amyloid plaque pathology,  
1306 with reduced plaque accumulation at later ages. **A** and **B**, Amyloid plaque was visualized using  
1307 the Campbell-Switzer silver stain method in non-transgenic (Ntg) controls or transgenic  
1308 PS2APP mice with either wild type (wt), heterozygous (het) or homozygous knockout (ko)  
1309 *Trem2* alleles. Quantification of the percent area covered by amyloid plaque was measured

1310 from coronal sections of indicated sex and age. Representative low (left, scale bar = 400  $\mu\text{m}$ )  
1311 and high (right, scale bar = 100  $\mu\text{m}$ ) magnification images of amyloid stains are shown. In the  
1312 absence of Trem2, plaque loads were elevated in 6-7mo females but reduced in 12mo females  
1313 and in 19-22mo males. See also Figure 3-1 for two-photon imaging of methoxy-X04-labeled  
1314 plaque in somatosensory cortex of 6mo females and 8mo males. **C**, The Campbell-Switzer  
1315 silver stain turns highly mature plaque cores amber (red arrowheads). Quantification plot (left)  
1316 and representative images (right, scale bar = 20  $\mu\text{m}$ ) of amber core frequency in 19-22mo male  
1317 mice. Bars represent mean  $\pm$  SEM. Significant differences between groups were determined by  
1318 unpaired t-test or ANOVA followed by Tukey's multiple comparison test (\* $p$ <0.05, \*\* $p$ <0.01,  
1319 \*\*\* $p$ <0.001, \*\*\*\* $p$ <0.0001 versus PS2APP;Trem2<sup>wt</sup> or as indicated).

1320

1321 **Figure 4.** Trem2 deletion impairs the consolidation of  $\beta$ -amyloid into dense plaque. **A**,  $\beta$ -  
1322 amyloid plaques were visualized by staining X-34 staining and confocal z-stack imaging.  
1323 Representative maximum projection images of X-34<sup>+</sup> plaques from 12mo PS2APP females of  
1324 different Trem2 genotypes are shown (top). High magnification images show a representative  
1325 plaque from each genotype with the outlined masks used to delineate the compact core (green)  
1326 and compact+diffuse (blue) areas of the plaque (bottom). Scale bars, 20  $\mu\text{m}$ . **B**, The  
1327 diffuseness index (see Methods) of the X-34<sup>+</sup> plaques in cohorts of the indicated age and sex  
1328 were quantified. Each data point represents one animal's plaque diffuseness index averaged  
1329 from 3-4 fields of view. Bars represent mean  $\pm$  SEM. Significant differences between groups  
1330 were determined by unpaired t-test or ANOVA followed by Tukey's multiple comparison test  
1331 (\*\* $p$ <0.01, \*\*\* $p$ <0.001, \*\*\*\* $p$ <0.0001 versus PS2APP;Trem2<sup>wt</sup> or as indicated).

1332

1333 **Figure 5.** Trem2 deletion increases the A $\beta$ 42:A $\beta$ 40 ratio and soluble fibrillar A $\beta$  oligomers in  
1334 PS2APP brains. **A** and **B**, Frozen hippocampal tissues were homogenized and processed for  
1335 measuring the abundance of A $\beta$ 40 and A $\beta$ 42 peptides by ELISA in the soluble (TBS) and  
1336 insoluble (GuHCl) fractions. The ratio of A $\beta$ 42:A $\beta$ 40 in the TBS (**A**) and GuHCl (**B**) fractions are  
1337 shown. Each data point represents one animal's A $\beta$ 42:A $\beta$ 40 ratio. For individual A $\beta$ 40 and A $\beta$ 42  
1338 peptide measurements, see Figure 5-1. **C**, Image of non-denaturing dot-blot of hippocampal  
1339 soluble TBS homogenates from 12mo female animals immunostained with the fibrillar  
1340 oligomeric A $\beta$  antibody OC (green) and control  $\beta$ -actin antibody (red). Squares outline  
1341 PS2APP;Trem2<sup>wt</sup> samples and circles outline PS2APP;Trem2<sup>ko</sup> samples. # identifies a control  
1342 sample from a PS2APP;Bace1<sup>ko</sup> mouse. **D**, Signal intensity ratios of OC antibody to actin

1343 antibody are plotted for the dot blot shown in **C**. The dotted line demarcates the OC:actin ratio  
 1344 for a control sample from a PS2APP;Bace1<sup>ko</sup> mouse. **E**, The A $\beta$ 42:A $\beta$ 40 ratio (from **A**) and  
 1345 normalized OC<sup>+</sup> dot blot signal (from **D**) in the TBS soluble fraction showed a significant positive  
 1346 correlation (linear regression; df(1,28) F=8.63, p<0.01). **F**, Same as **C**, except immunostained  
 1347 with pan-A $\beta$  antibody 6E10 (green) and control GAPDH antibody (red). **G**, Signal intensity ratios  
 1348 of A $\beta$  6E10 antibody to control GAPDH antibody are plotted for the dot blot shown in **F**. The  
 1349 PS2APP;Bace1<sup>ko</sup> control sample still has substantial 6E10 signal (see dotted line) since the N-  
 1350 terminal A $\beta$  residues recognized by 6E10 are present in soluble APP when  $\alpha$ -secretase is the  
 1351 responsible enzyme. **H**, The A $\beta$ 42:A $\beta$ 40 ratio (from **A**) and normalized A $\beta$  6E10 dot blot signal  
 1352 (from **G**) in the TBS soluble fraction showed a significant negative correlation (linear regression;  
 1353 df(1,28) F=4.98, p<0.05). Bars represent mean  $\pm$  SEM. Significant differences between groups  
 1354 were determined by unpaired t-test or ANOVA followed by Tukey's multiple comparison test  
 1355 (\*p<0.05, \*\*p<0.01, \*\*\*p<0.001, \*\*\*\*p<0.0001 versus PS2APP;Trem2<sup>wt</sup> or as indicated).

1356

1357 **Figure 6.** ApoE markedly accumulates on plaques and in microglia in PS2APP;Trem2<sup>ko</sup>  
 1358 females. **A**, Plaque-associated ApoE signal was quantified for each animal in each cohort using  
 1359 2-3 sections per animal, with each section having a range of ~50-800 plaques contributing to  
 1360 the analysis. Significant increases were observed in 6-7mo and 12mo female (f)  
 1361 PS2APP;Trem2<sup>ko</sup> mice but not in males (m). **B**, Representative low magnification images of the  
 1362 hippocampus (top row) and high magnification images of the subiculum (enlarged from the  
 1363 boxed regions) from 12mo female brain sections stained with methoxy-X04 to label plaque  
 1364 (blue), anti-Iba1 to label microglia (green), and anti-ApoE (red). Arrows point to examples of  
 1365 plaques with intense ApoE staining, which are atypical in Trem2<sup>wt</sup> females but typical in Trem2<sup>ko</sup>  
 1366 females at this age. **C**, Representative 20x maximum projection of confocal z-stacks imaged  
 1367 from cortex, highlighting ApoE (red) localization in microglia (Iba1, green) and plaque (blue).  
 1368 Microglia with small ApoE puncta (arrows) are typical in Trem2<sup>wt</sup>, while microglia with enlarged  
 1369 ApoE structures (arrowheads) are frequent in Trem2<sup>ko</sup>. Plaques with strong ApoE labeling are  
 1370 more common in Trem2<sup>ko</sup> (asterisks). **D**, Analysis of the fraction of Iba1 signal that overlaps  
 1371 with ApoE staining (Manders colocalization coefficient) in 12mo PS2APP females revealed  
 1372 increased colocalization in Trem2<sup>ko</sup> microglia. **E**, RNA-Seq profiles of microglia FACS-purified  
 1373 from brains of 14mo PS2APP mice showed no difference in *ApoE* expression between Trem2<sup>wt</sup>  
 1374 and Trem2<sup>ko</sup> microglia (MG). **F**, Expression profiles of microglia FACS-purified from brains of  
 1375 8mo non-transgenic or 5xFAD mice revealed strong *ApoE* induction by  $\beta$ -amyloid pathology in  
 1376 both Trem2<sup>wt</sup> and Trem2<sup>ko</sup> microglia, with induction in 5xFAD;Trem2<sup>ko</sup> relative to 5xFAD;Trem2<sup>wt</sup>

1377 microglia being 2-fold reduced in one dataset (GSE132508, RNA-Seq) and not significantly  
1378 different in another (GSE65067, microarray). Bars represent mean  $\pm$  SEM. Significant  
1379 differences between groups were determined by unpaired t-test or ANOVA followed by Tukey's  
1380 multiple comparison test (\* $p < 0.05$ , \*\* $p < 0.01$ , \*\*\*\* $p < 0.0001$  versus PS2APP;Trem2<sup>wt</sup> or as  
1381 indicated).

1382

1383 **Figure 7.** *Trem2* deletion exacerbates plaque-proximal axonal dystrophy. **A**, Representative  
1384 images from 12mo brain sections stained with methoxy-X04 to label plaque, anti-Iba1 to label  
1385 microglia, and anti-Lamp1 to label dystrophic axons around plaque. **B**, Microglial clustering  
1386 around plaque is impaired in *Trem2*-deficient mice. Plaque-associated Iba1 signal was  
1387 quantified for each animal in each cohort using 2-3 sections per animal, with each section  
1388 having hundreds or thousands of plaques contributing to the analysis. **C**, Axonal dystrophy per  
1389 plaque is exacerbated in *Trem2*-deficient mice. Plaque-associated Lamp1 signal was quantified  
1390 for each animal in a similar manner as Iba1 signal in panel B. **D**, Total axonal dystrophy is  
1391 exacerbated in *Trem2*-deficient mice. Total Lamp1 signal in each section was quantified, and  
1392 each data point represents the average score from 2-3 sections per animal. Bars represent  
1393 mean  $\pm$  SEM. Significant differences between groups were determined by unpaired t-test or  
1394 ANOVA followed by Tukey's multiple comparison test (\*\* $p < 0.01$ , \*\*\* $p < 0.001$ , \*\*\*\* $p < 0.0001$   
1395 versus PS2APP;Trem2<sup>wt</sup> or as indicated).

1396

1397 **Figure 8.** Disintegrative degeneration staining and CSF NfL measurements reveal exacerbated  
1398 neuronal damage in *Trem2*-deficient mice at later ages. **A**, Quantification of sections from non-  
1399 transgenic (Ntg) and PS2APP mice with indicated *Trem2* genotypes stained using an amino-  
1400 cupric-silver staining method that labels degenerative neuronal processes. Each data point  
1401 represents the average %area covered/section for ~10 sections per animal. **B**, Representative  
1402 low (left, scale bar = 400  $\mu$ m) and high (right, scale bar = 100  $\mu$ m) magnification images from  
1403 the 12mo female and 19-22mo male cohorts are shown. Degenerative signal is apparent in  
1404 plaque-accompanying foci (red arrowheads) throughout the cortex and hippocampus and in  
1405 certain white matter tracts including the corpus callosum (cc). **C**, Plasma (left) and CSF (right)  
1406 NfL was measured from a separate, mixed sex cohort of 12mo PS2APP;Trem2<sup>wt</sup> and  
1407 PS2APP;Trem2<sup>ko</sup> mice. Bars represent mean  $\pm$  SEM. Significant differences between groups  
1408 were determined by unpaired t-test or ANOVA followed by Tukey's multiple comparison test  
1409 (\*\* $p < 0.01$ , \*\*\*\* $p < 0.0001$  versus PS2APP;Trem2<sup>wt</sup> or as indicated).

1410

1411 **Figure 9.** *Trem2* deletion exacerbates dendritic spine loss near plaque. **A**, Intact brains from  
1412 6mo female PS2APP mice with wild type (wt), knockout (ko), or heterozygous (het) *Trem2*  
1413 genotypes and carrying the Thy1::GFP-M transgene, which sparsely labels excitatory cortical  
1414 neurons, were imaged in the somatosensory cortex using two-photon microscopy. Dendritic  
1415 shafts proximal to plaque (within 20  $\mu\text{m}$ ) or distally located ( $\geq 100 \mu\text{m}$  from any plaque) were  
1416 imaged, with representative images shown. **B**, Each data point represents the average of five  
1417 spine density measurements from one animal. Spine density was ~50% reduced on plaque-  
1418 proximal dendrite segments relative to distal dendrite segments from the same animals. Spine  
1419 density near plaque was lower in PS2APP;*Trem2*<sup>ko</sup> mice than in PS2APP;*Trem2*<sup>wt</sup> or  
1420 PS2APP;*Trem2*<sup>het</sup> mice. Bars represent mean  $\pm$  SEM. Significant differences between groups  
1421 were determined by ANOVA (\* $p < 0.05$ , \*\* $p < 0.01$ ). Spine volume was unaffected by either plaque  
1422 proximity or *Trem2* genotype (data not shown).

1423

1424

#### 1425 EXTENDED DATA LEGENDS

1426

1427 **Figure 1-1.** Gliosis and engagement/uptake of plaque by microglia are reduced in *Trem2*-  
1428 deficient mice. **A**, Immunohistochemical stains for Iba1 demonstrated a significant reduction in  
1429 Iba1<sup>+</sup> area per section in *Trem2*-deficient mice. Representative Iba1 stains for the 12mo cohort  
1430 are shown in Fig. 1B. **B**, (Top) Immunohistochemical stains for Gfap demonstrated a significant  
1431 reduction in Gfap<sup>+</sup> area per section, suggestive of reduced astrogliosis, in *Trem2*-deficient mice.  
1432 (Bottom) Representative low (left, scale bar = 400  $\mu\text{m}$ ) and high (right, scale bar = 100  $\mu\text{m}$ )  
1433 magnification images of Gfap<sup>+</sup> staining in the 12mo cohort are shown. **C**, Confocal z-stack  
1434 images from 12mo female PS2APP cortical tissue were stained for microglia using anti-Iba1 and  
1435 for plaque using methoxy-X04. Stark reductions in overlap were observed in *Trem2*-deficient  
1436 mice using Manders' colocalization coefficients, corroborating the finding in Fig. 1G,H that  
1437 detection of methoxy-X04<sup>+</sup> staining was reduced in PS2APP;*Trem2*<sup>ko</sup> compared to  
1438 PS2APP;*Trem2*<sup>wt</sup> microglia dissociated from brains and measured by flow cytometry. Bars and  
1439 lines represent mean  $\pm$  SEM. Significant differences between groups were determined by  
1440 unpaired t-test, or by ANOVA followed by Tukey's multiple comparison test when more than two  
1441 groups were compared (\* $p < 0.05$ , \*\* $p < 0.01$ , \*\*\* $p < 0.001$ , \*\*\*\* $p < 0.0001$  versus PS2APP;*Trem2*<sup>wt</sup>  
1442 or as indicated).

1443

1444 **Figure 2-1.** Extended data table relating to Figure 2, with genome-wide RNA-Seq expression  
1445 profiles and differential expression statistics for resident myeloid cells ( $Iba1^+CD45^+CCR2^-Ly6g^-$ )  
1446 FACS-purified from dissociated brains (cortex and hippocampus) of PS2APP;Trem2<sup>wt</sup> (n=7, 5  
1447 females and 2 males) and PS2APP;Trem2<sup>ko</sup> (n=6, 5 females and 1 male) at ~14 months of age.  
1448 Raw RNA-Seq data files have been deposited to NCBI GEO under accession number  
1449 GSE140744.

1450  
1451 **Figure 2-2.** Induction of genes related to proliferation and Wnt-related signaling exhibit Trem2-  
1452 dependence in multiple  $\beta$ -amyloidosis models. **A**, Gene ontology (GO) analysis implicated  
1453 several biological processes whose induction was impaired in the absence of *Trem2*, based on  
1454 overrepresentation of the genes listed for a given process (false discovery rate (FDR)  $\leq 0.05$ )  
1455 among the list of 144 transcripts with at least 2-fold reduced abundance (adjusted  $p \leq 0.05$ ) in  
1456 PS2APP;Trem2<sup>ko</sup> vs. PS2APP;Trem2<sup>wt</sup> microglia. **B**, Nine genes featured in Fig. 2B,C that had  
1457 shown reduced expression in PS2APP;Trem2<sup>ko</sup> microglia were analyzed in a separate dataset  
1458 from independent researchers (GSE132508) for whether their expression was also reduced in  
1459 Trem2<sup>ko</sup> relative to Trem2<sup>wt</sup> microglia, FACS-purified from 8-month 5xFAD mouse brains.  
1460 Expression profiles for microglia from 8-month non-transgenic (Ntg) mice are also shown as a  
1461 point of reference to visualize the extent of gene induction in 5xFAD;Trem2<sup>wt</sup> versus  
1462 Ntg;Trem2<sup>wt</sup> microglia. Conservation of Trem2-dependence between models was observed for  
1463 all except *Ptk7*. Bars and lines represent mean  $\pm$  SEM. Significant differences between  
1464 5xFAD;Trem2<sup>ko</sup> and 5xFAD;Trem2<sup>wt</sup> microglia were determined by unpaired t-test (\* $p < 0.05$ ,  
1465 \*\* $p < 0.01$ , \*\*\*\* $p < 0.0001$ ). Note: These statistics are not from a genome-wide analysis of  
1466 differential gene expression. **C**, The Proliferation microglial gene expression module (defined in  
1467 Friedman et al., 2018) was analyzed for induction in 5xFAD;Trem2<sup>wt</sup> microglia relative to  
1468 Ntg;Trem2<sup>wt</sup> microglia from non-transgenic mice and whether that induction was compromised  
1469 in 5xFAD;Trem2<sup>ko</sup> microglia. This corroborated similar findings from Fig. 2D in the PS2APP  
1470 model. Lines represent mean  $\pm$  SEM. Significant differences between groups were determined  
1471 by ANOVA followed by Tukey's multiple comparison test (\*\*\*\* $p < 0.0001$  as indicated).

1472  
1473 **Figure 2-3.** Gene expression modules change in PS2APP microglia, with Neurodegeneration-  
1474 related and Proliferation gene sets showing Trem2-dependence (related to Fig. 2D). The left  
1475 side of these heatmaps show how the expression of several microglial gene expression  
1476 modules changes in microglia FACS-purified from PS2APP versus non-transgenic (Ntg) brains,  
1477 using expression data from GSE89482. The right side of the heatmaps shows whether these

1478 changes in gene expression were affected by *Trem2* genotype in the current dataset. Induction  
1479 of the Neurodegeneration-related and Proliferation modules was impaired in *Trem2*<sup>ko</sup> microglia,  
1480 while the other modules were expressed to similar extents in PS2APP;*Trem2*<sup>ko</sup> and  
1481 PS2APP;*Trem2*<sup>wt</sup> microglia. Each row represents one gene in a module, each column is one  
1482 animal's microglial expression profile, and coloring represents Z-score of a sample's nRPKM  
1483 value for a given gene relative to average expression for that gene across all samples within a  
1484 study (not across studies, since libraries were prepared using different methods and nRPKM  
1485 values between studies are not directly comparable). Overall expression scores for each gene  
1486 set in each sample are plotted in Fig. 2D.

1487

1488 **Figure 3-1.** *Trem2* deletion increases plaque number in 6-month female somatosensory cortex.  
1489 6mo PS2APP females (**A**) or 8mo PS2APP males (**B**) with wild type (wt), knockout (ko), or  
1490 heterozygous (het) *Trem2* genotypes were i.p. injected with methoxy-X04 to label brain amyloid  
1491 content one day before tissue collection. Brains were perfused, fixed, and embedded in agarose  
1492 for en bloc two-photon imaging of intact somatosensory cortex (~200  $\mu$ m depth) and  
1493 quantitation of amyloid plaque content. Representative images are shown at left, with plots of  
1494 plaque count per cubic millimeter shown to the right and each data point representing  
1495 measurement from one animal. The brains used in **A** were the same brains used for dendritic  
1496 spine measurements in Figure 8. Bars and lines represent mean  $\pm$  SEM. Significant differences  
1497 between groups were determined by ANOVA followed by Tukey's multiple comparison test  
1498 (\*\*p<0.001, \*\*\*\*p<0.0001 versus PS2APP;*Trem2*<sup>wt</sup> or as indicated).

1499

1500 **Figure 5-1.** Reduced abundance of A $\beta$ 40 is more frequent than increased abundance of A $\beta$ 42  
1501 in *Trem2*-deficient PS2APP mouse brains. Frozen hippocampal tissues from cohorts of  
1502 PS2APP mice with indicated age, sex, and *Trem2* genotype were homogenized in TBS, and the  
1503 abundance of A $\beta$  peptides in the TBS-soluble (**A**) and guanidine HCl (GuHCl)-soluble (**B**)  
1504 fractions was measured by ELISA assays specific for detecting A $\beta$ 40 (top row) or A $\beta$ 42 (bottom  
1505 row). Bars and lines represent mean  $\pm$  SEM. Significant differences between groups were  
1506 determined by unpaired t-test or ANOVA followed by Tukey's multiple comparison test (\*p<0.05,  
1507 \*\*p<0.01, \*\*\*p<0.001, \*\*\*\*p<0.0001 versus PS2APP;*Trem2*<sup>wt</sup> or as indicated).

FIGURE 1

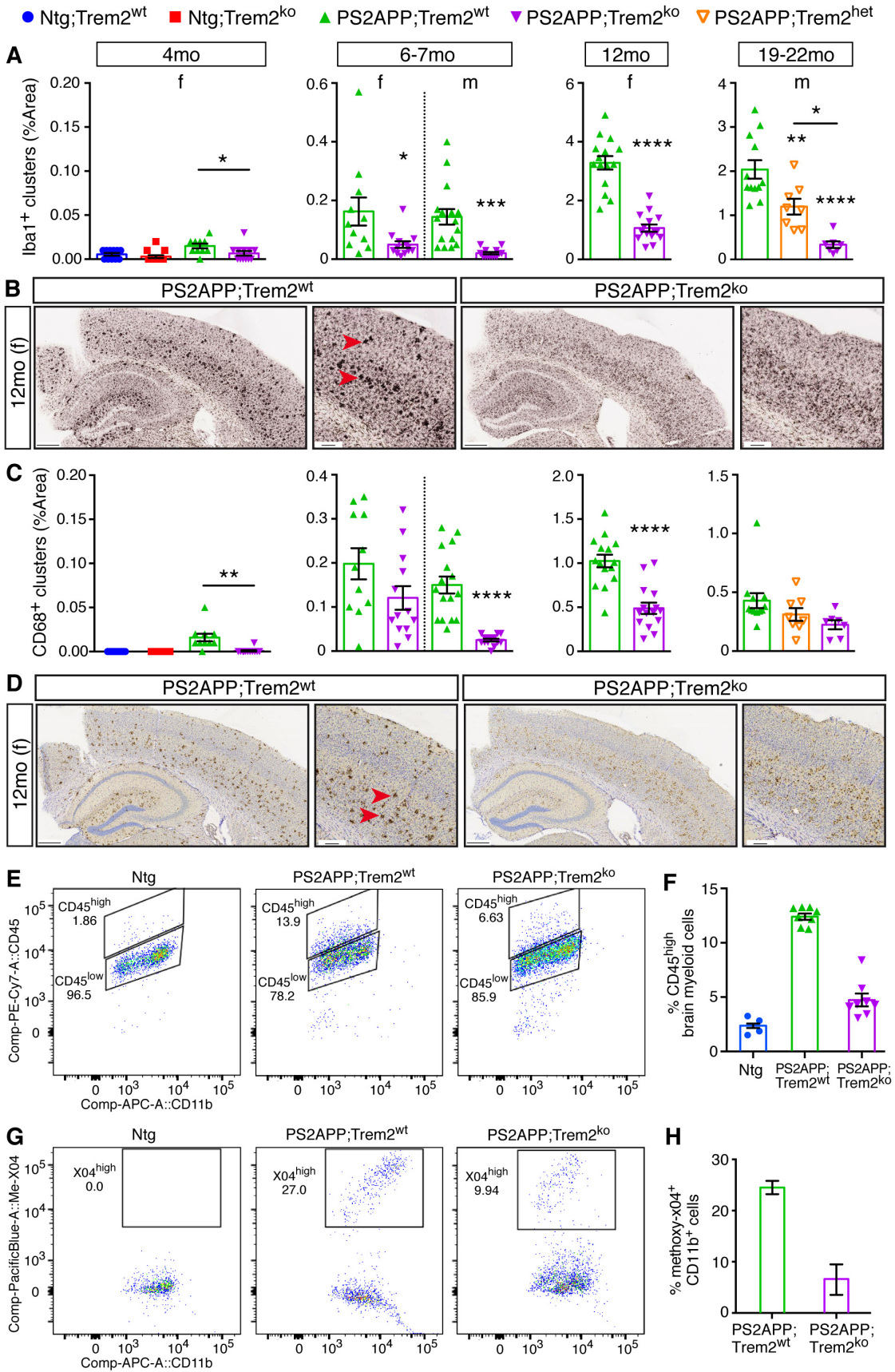


FIGURE 2

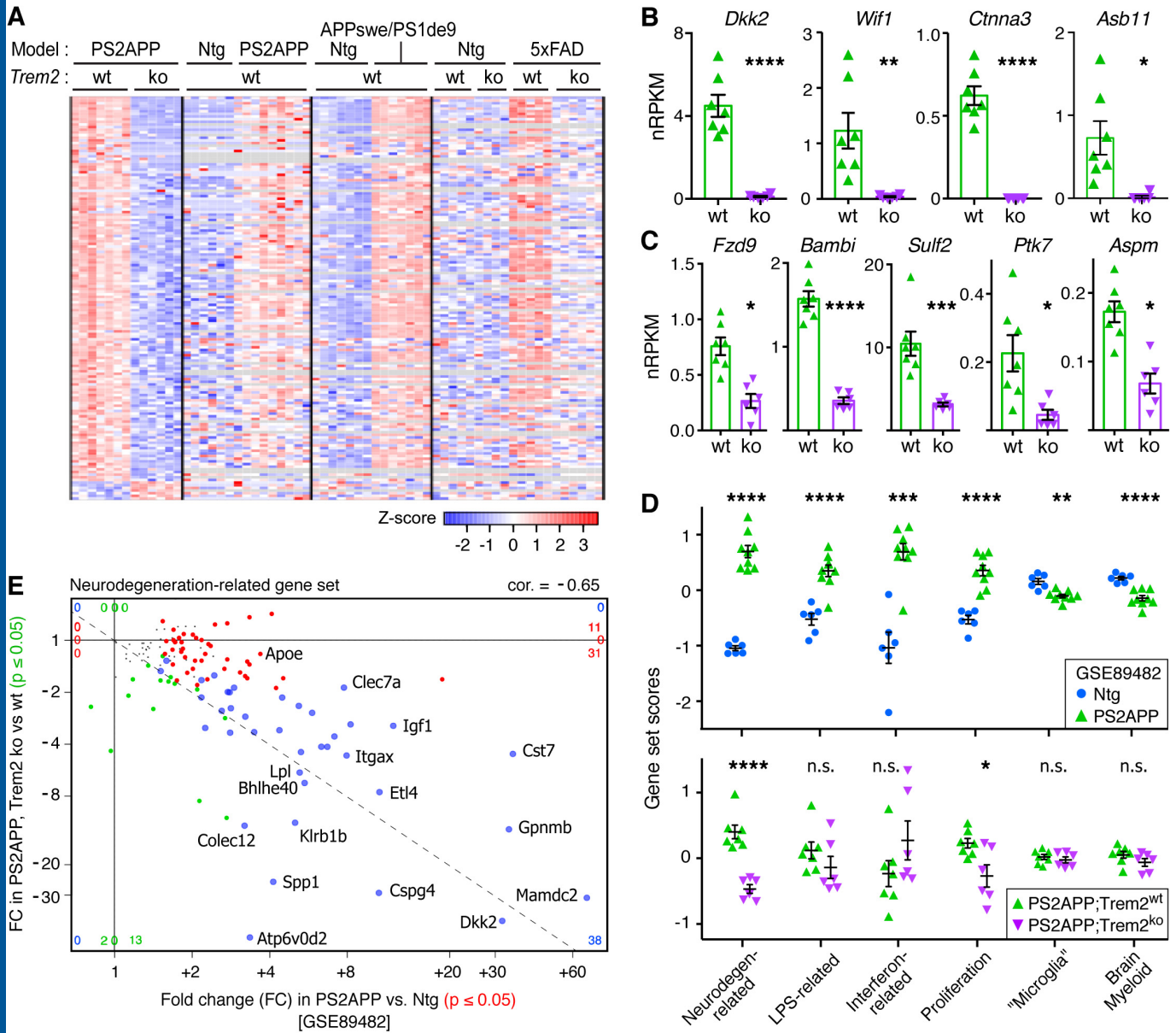


FIGURE 3

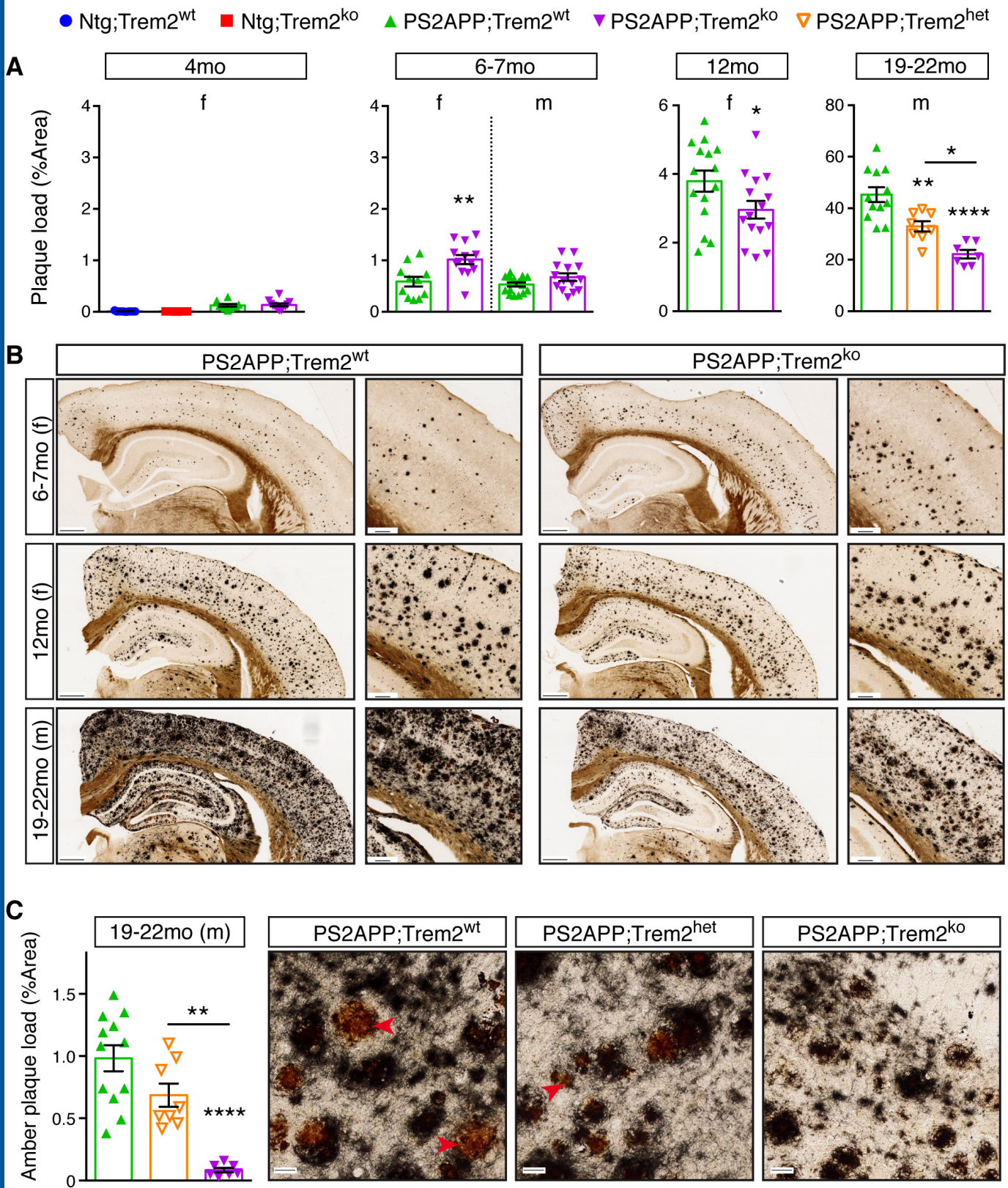


FIGURE 4

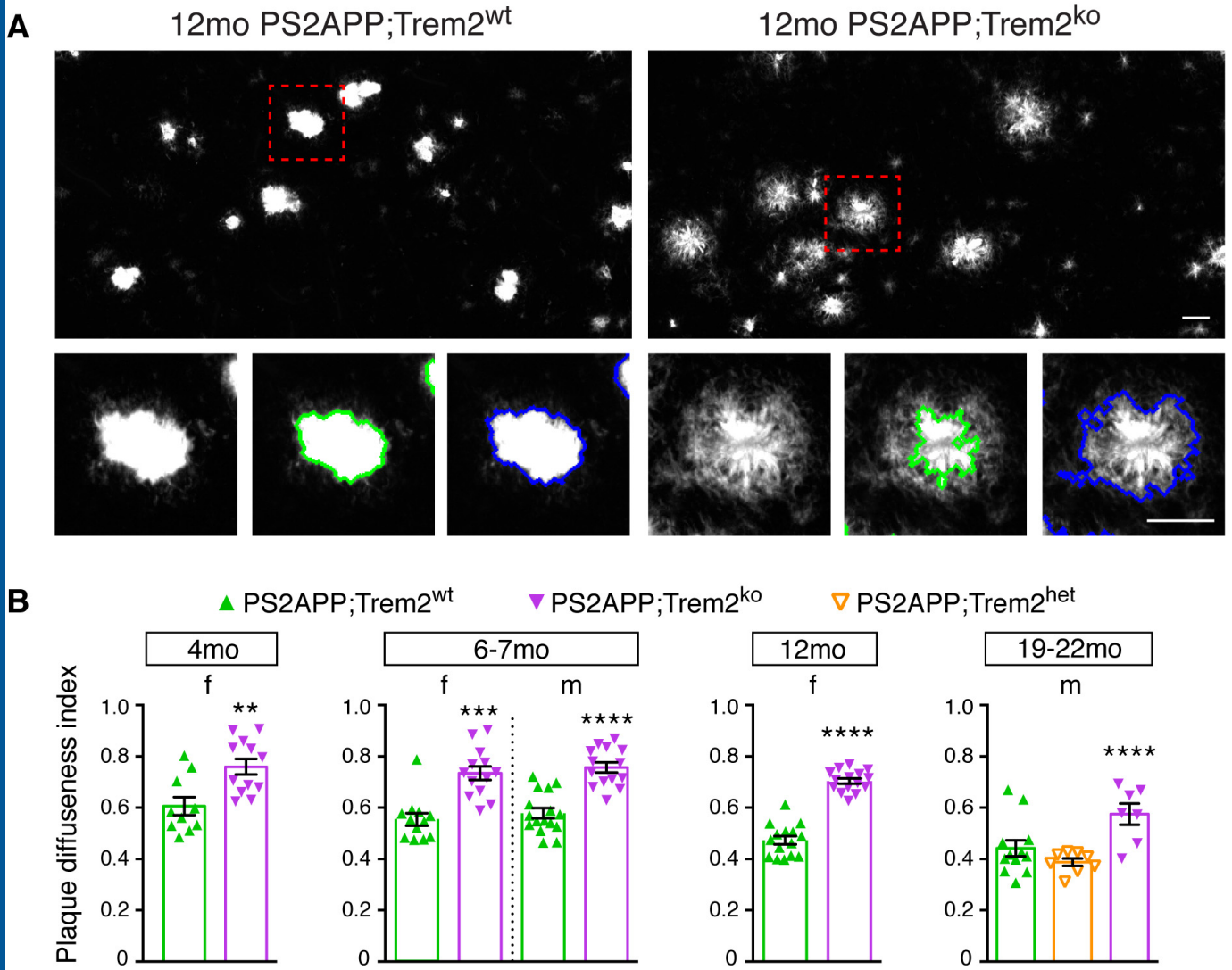


Figure 5

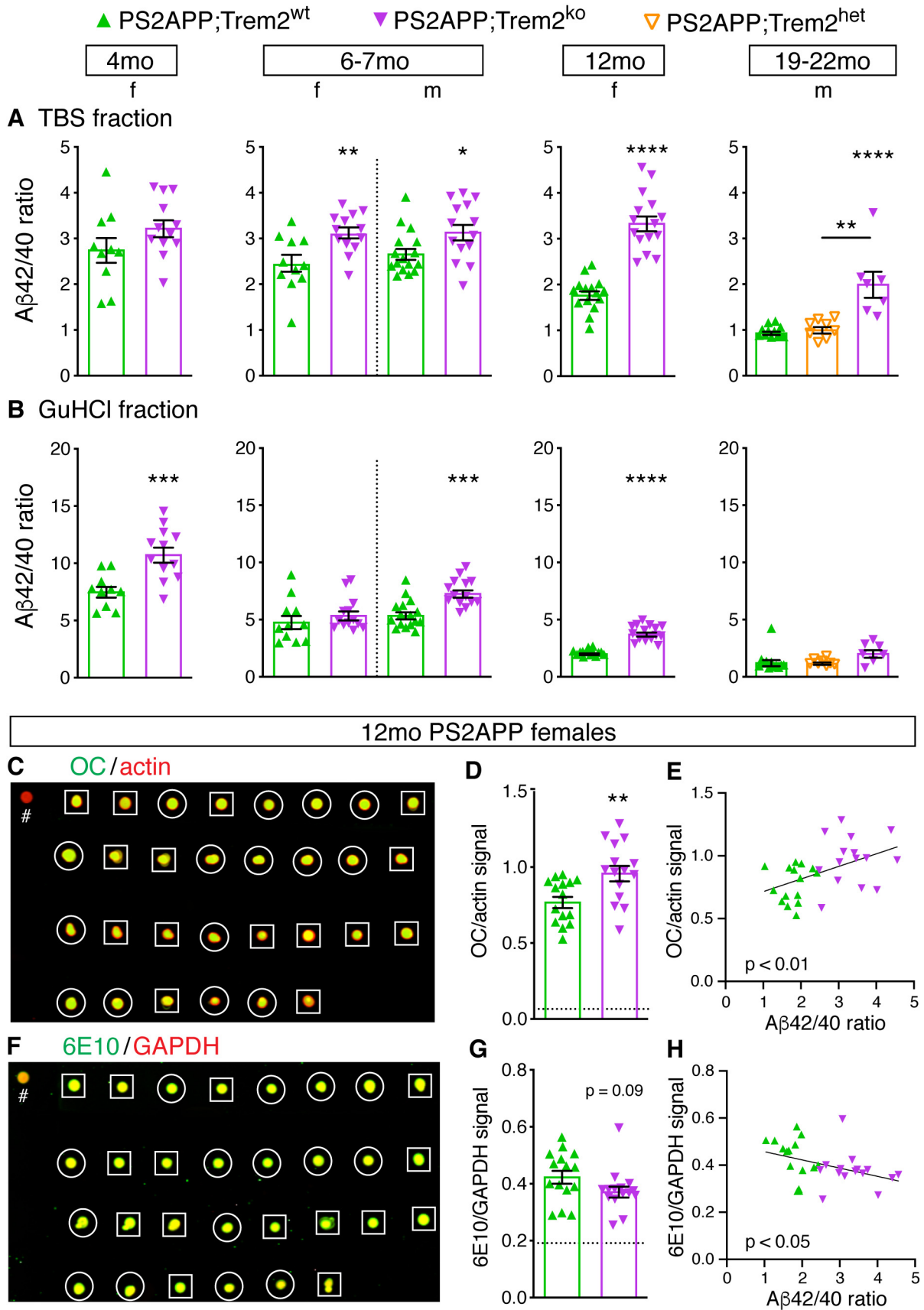
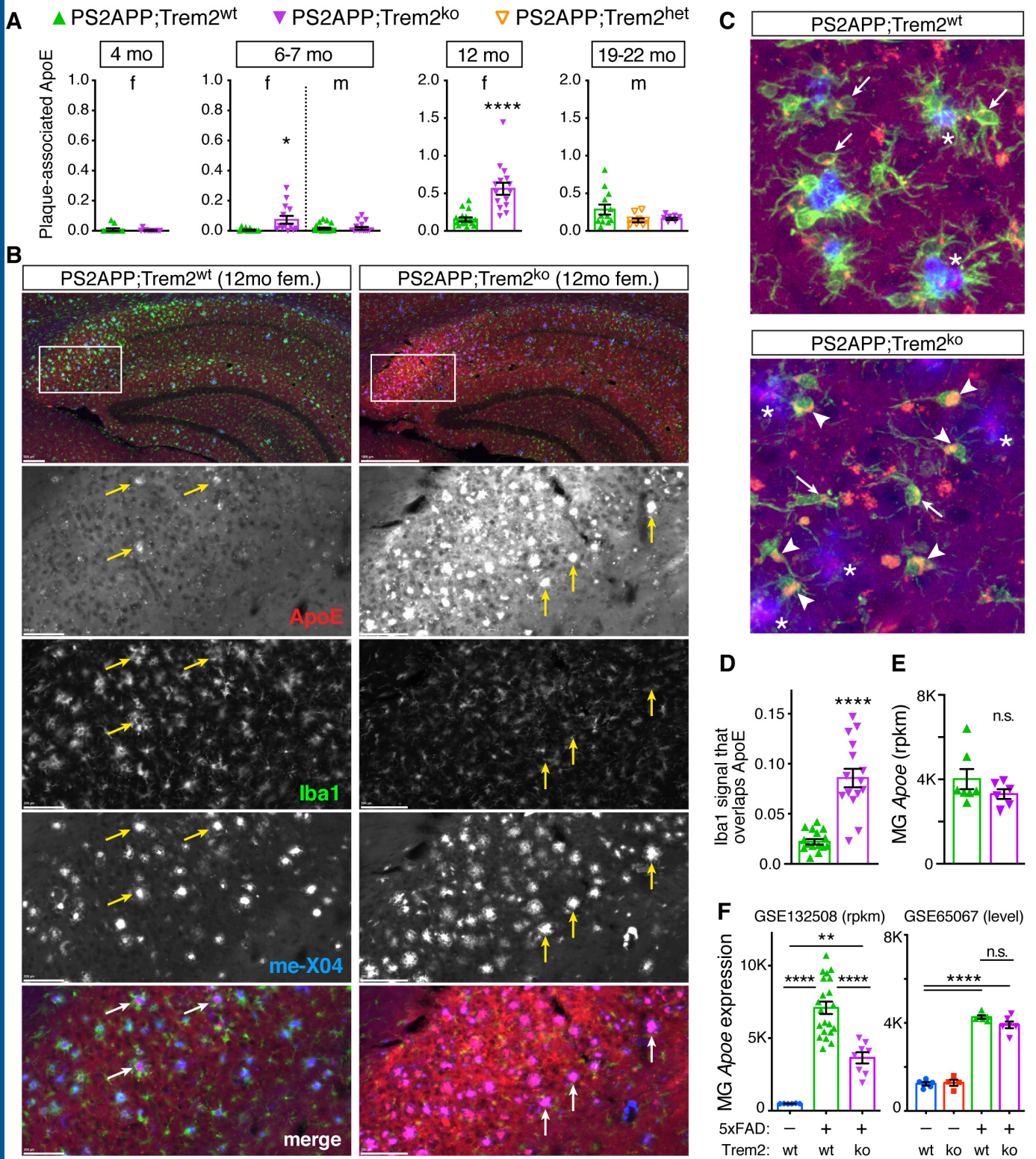


FIGURE 6



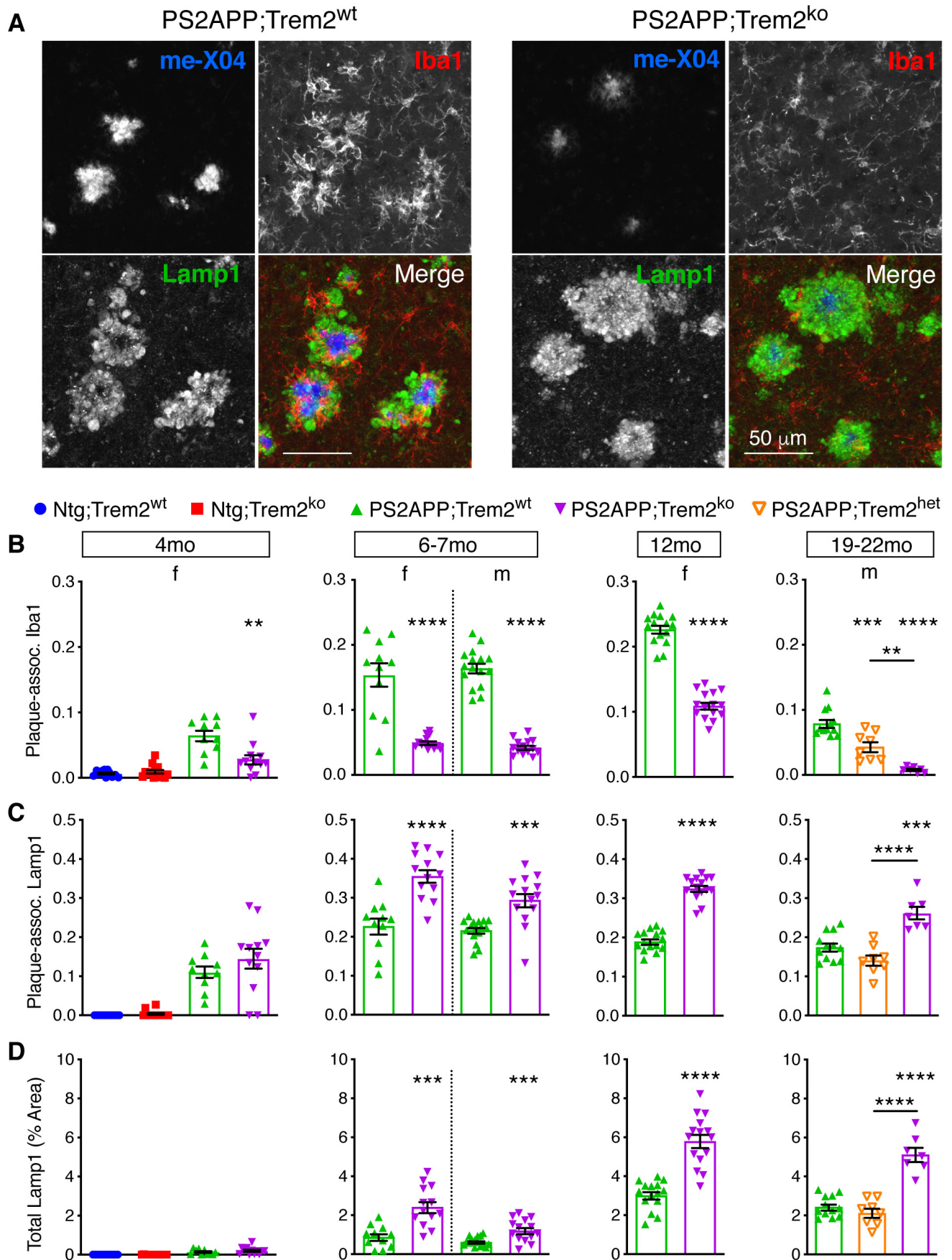


FIGURE 8

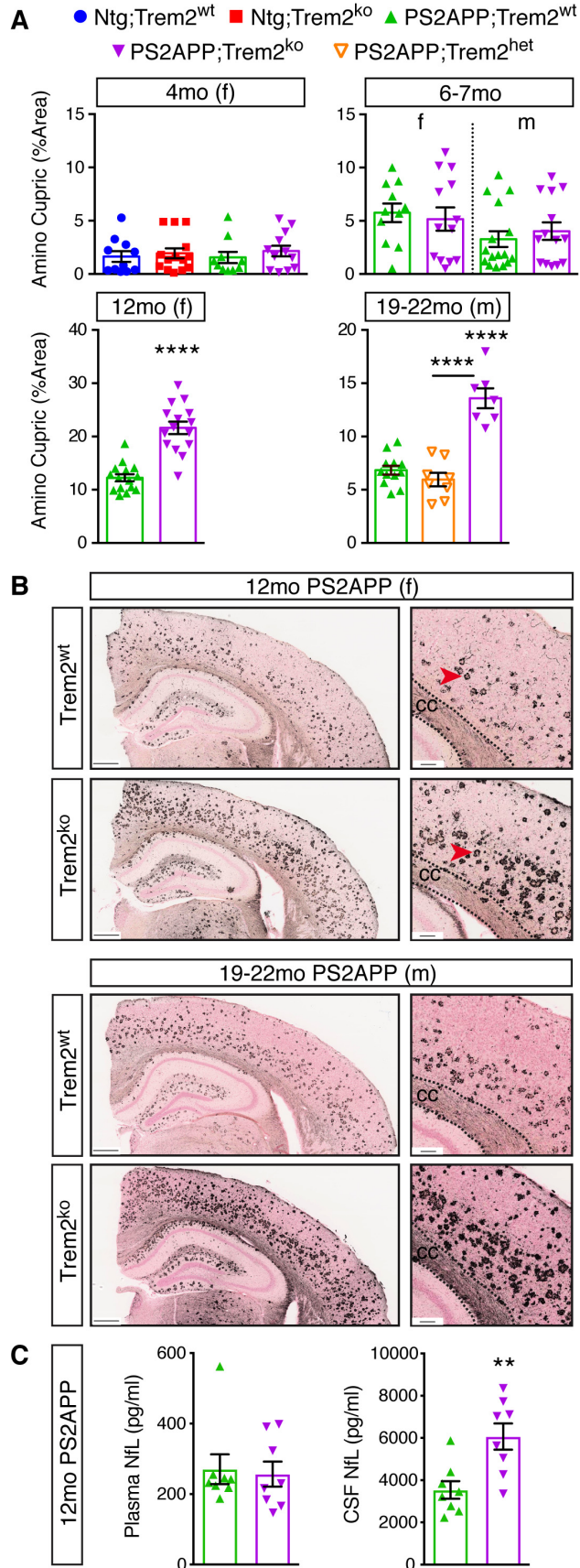


FIGURE 9

